

Thermoelectric transport of strained CsK₂Sb: Role of momentum-dependent scattering in low-dimensional Fermi surfaces

Øven A. Grimenes,^{1,*} G. Jeffrey Snyder,² Ole M. Løvvik,³ and Kristian Berland^{1,†}

¹*Department of Mechanical Engineering and Technology Management,
Norwegian University of Life Sciences, NO-1432 Ås, Norway*

²*Materials Science and Engineering, Northwestern University, Evanston, Illinois 60208, USA*

³*SINTEF Sustainable Energy Technology, Forskningsveien 1, NO-0314 Oslo, Norway*

(Dated: December 3, 2024)

In this first-principles study, we investigated the thermoelectric properties of the full-Heusler compound CsK₂Sb at different compressive strains. We predict a p-type figure of merit (zT) of 2.6 at 800 K, in line with previous high zT predictions. This high zT arises from a low lattice thermal conductivity of $0.35 \text{ W m}^{-1} \text{ K}^{-1}$ and a valence band structure exhibiting significant effective mass anisotropy, forming tube-like energy isosurfaces below the band edge, a characteristic of two dimensional (2D) systems that leads to a large number of high mobility charge carriers. The extended energy isosurfaces also correspond to large electron-scattering space, but with realistic wave function- and momentum-dependent electron scattering, we found this effect to be largely compensated by reduced scattering rates for larger momentum \mathbf{q} . The electronic transport properties were further enhanced with compressive strain, increasing the power factor by up to 66%, in part due to enhanced 2D-features of the valence band. Unfortunately, compressive strain also increase the lattice thermal conductivity, resulting in a maximum p-type $zT = 2.7$ at 1% compressive strain. In the conduction band, strain can align the Γ - and X-centered valleys, resulting in the optimal n-type zT increasing from 0.9 to 2.3 when adding 2% compressive strain. Thus, the material class can have potential for both good p- and n-type thermoelectricity.

I. INTRODUCTION

The ability to convert heat to electricity and vice versa makes thermoelectric (TE) materials useful for energy harvesting and distributed cooling [1, 2]. With higher efficiency, they could see more widespread use, such as for waste-heat recovery, geothermal systems, or combined electricity and heat generators[3, 4], which could be key in the ongoing green-energy transition. Enhancing the TE efficiency is, however, highly nontrivial, as expressed by the TE figure of merit of a material, $zT = S^2 \sigma T / (\kappa_e + \kappa_\ell)$. Here, S is the Seebeck coefficient, σ the electrical conductivity, T the temperature, and κ_e and κ_ℓ the electron and lattice thermal conductivity, respectively. These parameters are highly interdependent; increasing σ typically decreases S and increases κ_e . Reducing κ_ℓ through increased phonon scattering can also inadvertently reduce σ .

A wide range of strategies to reach higher zT has been proposed and investigated. Starting from promising materials discovered through experimental and computational studies, the lattice thermal conductivity can be reduced by isovalent alloying to selectively scatter phonons more than electrons[5], or employ nanostructuring which impedes phonons with long mean free path (MFP) compared to short-MFP electrons[6]. Electronic transport properties can be enhanced by increasing the number of degenerate conduction or valence bands valleys through strain[7, 8] and alloying[9, 10], but also by

introducing resonance states[11–13], or interfacial effects described as energy filtering [14–16]. It was also suggested that low dimensional materials can exhibit enhanced density of states (DOS) near the Fermi level, greatly enhancing S [17, 18], while also reducing κ_ℓ but has been shown to actually reduce PF when multiple subbands are considered[19, 20]. The practical realization of such low-dimensional band structures has typically been associated to low-dimensional materials such as superlattice structures, which necessitates the need for complex processing methods such as molecular beam epitaxy[21]. Encouragingly, several recently identified materials possess low-dimensional features in the band structure despite being bulk, 3D isotropic materials. Such materials can exhibit Fermi surfaces consisting of tubes (2D), as seen in Figure 3, and sheets (1D) rather than spheres that arise in traditional, 3D parabolic band structures [22–26].

Computational transport calculations are playing an increasingly important role in the quest for higher zT , not only for optimizing material properties such as the doping level ε_F , but also for identifying novel high- zT materials. Such studies have typically been based on first-principles simulations based on density functional theory (DFT) and in turn solving the semi-classical Boltzmann transport equation. Due to the complexity of computing the relaxation time τ , the constant relaxation time approximation (CRTA) remains widely used, particularly in screening studies [27–32].

For complex, low-dimensional band structures, high zT predictions are often attributed to obtaining simultaneously a high DOS and high group velocities[23, 33]. However, earlier computational studies have usually been

* oven.andreas.grimenes@nmbu.no

† kristian.berland@nmbu.no

based on the CRTA or energy-dependent approximation for $\tau = \tau(E)$ [22, 23, 26]. Recent studies have highlighted the importance of fully accounting for the scattering, with findings such as significantly reduced inter-valley compared to intra-valley scattering[34, 35]. Only a handful of studies have discussed the effect of low-dimensional band structures on the electronic transport properties beyond the CRTA or other simple approximations[25, 33, 36]. Identifying materials with low-dimensional band structures and favorable scattering characteristics could lead to novel outstanding TE materials.

Among the A_3Sb group of materials, where A is an alkali metal, several exhibit low-dimensional band structures[37–39]. One such material is the full-Heusler CsK_2Sb (sometimes denoted K_2CsSb), which is a known photocathode[40, 41]. So far, there are four first-principles TE studies beyond the CRTA on this compound[42–45]. While all studies report ultra-low values of κ_ℓ , their electron transport results are somewhat contradictory. Sharma et al.[45] predicting the material to be superior as n-type TE, while Yue et al.[42] and Yuan et al.[43] finds stronger p-type performance.

In this study, we computed the transport properties of CsK_2Sb and performed an in-depth analysis of the electron scattering of the compound. In particular, we investigated the effect of compressive strain on the electronic and lattice TE properties, as it allowed us to tune the low dimensionality of the valence band and align the conduction band valleys.

II. METHODS

A. Electron transport

Electron transport properties were calculated with the AMSET code[46], based upon BoltzTraP2[47], which solves the Boltzmann's transport equation in the relaxation time approximation. At this level of theory, the transport properties depend on the transport distribution function, as follows

$$\Sigma(\varepsilon) = \int_{BZ} \frac{d\mathbf{k}}{8\pi^3} \sum_n \mathbf{v}_{n\mathbf{k}} \otimes \mathbf{v}_{n\mathbf{k}} \tau_{n\mathbf{k}} \delta(\varepsilon - \varepsilon_{n\mathbf{k}}), \quad (1)$$

where $\delta(\varepsilon - \varepsilon_{n\mathbf{k}})$ is the Dirac delta function, $\mathbf{v}_{n\mathbf{k}}$ is the electron group velocity, and $\tau_{n\mathbf{k}}$ is the relaxation time for a given band n and \mathbf{k} -point \mathbf{k} . ε indicates carrier energies. For electron transport, $\Sigma(\varepsilon)$ is weighted by the (Fermi) selection functions,

$$W^{(\alpha)}(\varepsilon) = (\varepsilon - \varepsilon_F)^\alpha \left(\frac{-\partial f(\varepsilon)}{\partial \varepsilon} \right), \quad (2)$$

where ε_F is the chemical potential, and f is the equilibrium Fermi-Dirac distribution function around ε_F at a given temperature T . The selection functions for

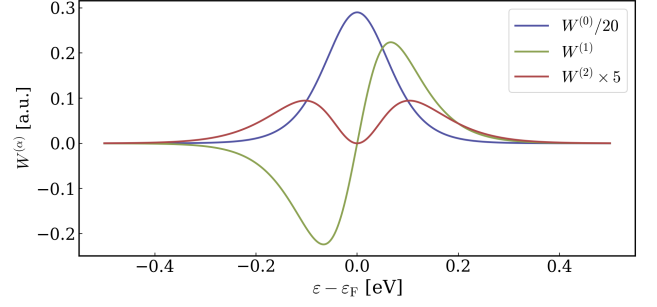


FIG. 1. Selection functions for $\alpha = 0, 1, 2$ at $T = 500$ K. $W^{(0)}$ and $W^{(2)}$ are scaled down and up, respectively, for easier comparison.

$\alpha = 0, 1, 2$ are shown in Fig. 1. The thermoelectric properties can be obtained from the generalized transport coefficients

$$\mathcal{L}^{(\alpha)}(\varepsilon_F) = q^2 \int_{-\infty}^{\infty} \Sigma(\varepsilon) W^{(\alpha)}(\varepsilon) d\varepsilon, \quad (3)$$

where q is the elementary charge. In turn, σ , S , and κ_e are given as

$$\sigma = \mathcal{L}^{(0)}, \quad (4)$$

$$S = \frac{\mathcal{L}^{(1)}}{qT\mathcal{L}^{(0)}}, \quad (5)$$

$$\kappa_e = \frac{1}{q^2T} \left[\mathcal{L}^{(2)} - \frac{(\mathcal{L}^{(1)})^2}{\mathcal{L}^{(0)}} \right]. \quad (6)$$

The electronic relaxation time is in AMSET calculated as the inverse of the total scattering rate $\tau_{n\mathbf{k}} = 1/\Gamma_{n\mathbf{k}}^{\text{Tot}}$ which is the sum of the scattering rates from acoustic deformation potential (ADP) scattering, polar optical phonon (POP) scattering, ionized impurity (IMP) scattering, and piezoelectric (PIE) scattering [46]:

$$\Gamma_{n\mathbf{k}}^{\text{Tot}} = \Gamma_{n\mathbf{k}}^{\text{ADP}} + \Gamma_{n\mathbf{k}}^{\text{PIE}} + \Gamma_{n\mathbf{k}}^{\text{POP}} + \Gamma_{n\mathbf{k}}^{\text{IMP}}. \quad (7)$$

These scattering rates depend on the deformation potential $D_{n\mathbf{k}}$, the elastic tensor C_{ij} , the piezoelectric tensor, the static ϵ_s and high frequency ϵ_∞ dielectric tensor, the weighted polar optical phonon frequency ω_{po} , the band structure, and the wave functions computed from first principles. AMSET is also used to set up the structural deformations needed to obtain the deformation potential. ω_{po} is calculated for the Γ -point phonon frequencies and Born effective charges. Details about this methodology and expressions for the scattering rates can be found in Appendix A and Ref. [46].

B. Computational details

The properties needed for the AMSET transport calculations were predicted with density functional theory

(DFT) calculations as implemented in VASP[48, 49]. The vdW-DF-cx[50, 51] functional was used due to its generally accurate bulk modulus and lattice constants of solids[50–53], with auxiliary calculations using the HSE06[54] hybrid functional for benchmarking. A plane wave energy cutoff of 520 eV was used and the number of electrons states for the basis set was 9 (Cs), 9 (K), and 5 (Sb); both in compliance with the standard settings of Materials Project (MP)[55]. The initial crystal structure was retrieved from the MP database (mp-581024) and relaxed on a $10 \times 10 \times 10$ k-points grid until forces fell below 5.0×10^{-5} eV/Å. A second ionic relaxation was subsequently performed to remove Pulay stress. Density functional perturbation theory (DFPT) calculations with VASP[56] were used to compute the dielectric constants, Born effective charges, and Γ -point phonon frequencies, while the elastic constants were calculated using finite differences[57]. For both of these calculations, a \mathbf{k} -point grid of $12 \times 12 \times 12$ was used. For each strain, the relevant properties were computed at the equivalent external pressure (separately determined with DFT). A $20 \times 20 \times 20$ \mathbf{k} -point grid interpolated to a $53 \times 53 \times 53$ grid in AMSET was used for transport calculations, while the deformation potential was extracted using a $12 \times 12 \times 12$ \mathbf{k} -points grid.

The lattice thermal conductivity κ_ℓ was calculated using the stochastic temperature-dependent effective potential method (sTDEP)[58] as implemented in the TDEP code[59]. Forces were calculated with VASP at the same level of theory and with the same numerical settings as the electron transport calculations, except using a lower \mathbf{k} -point density ($2 \times 2 \times 2$) for the supercell configuration calculations. Stochastic sampling of atomistic configurations was based on the Debye model and was used as the initial input to an iterative self-consistent calculation of force constants. Second- and third-order force constants were in each step extracted from displacement-force data using DFT as implemented in VASP for the force calculations. These force constants generated a new generation of configurations for new force calculations. The criterion for self-consistency was a difference in the phonon free energy of less than 1 meV/atom between two consecutive steps. The configurations consisted of 152 atoms in non-diagonal supercells with a spatial filling ratio of 99.5% of the ideal cube. The cutoff radius for extracting force constants was half of the supercell lattice constant (the maximum possible value). This cutoff gave, respectively, 41 and 821 irreducible second- and third-order force constants. The total number of configurations depended on the number of iterations, with an overdetermination ratio (the number of force data points divided by the number of irreducible force constants; a value of 10 is usually sufficient) of at least 111 (23) for determining force constants up to the second (third) order. The \mathbf{q} -point grid used to calculate κ_ℓ was varied between $15 \times 15 \times 15$ and $25 \times 25 \times 25$ and extrapolated to infinity, using the linear dependency between κ_ℓ and the reciprocal number of \mathbf{q} -points in each direction.

III. RESULTS

A. Materials properties

The lattice constant of CsK₂Sb was relaxed to 8.57 Å with DFT (at $T = 0$ K). With thermodynamic data from TDEP, we predicted the room temperature (300 K) lattice constant to be 8.623 Å, in excellent agreement with the experimental value of 8.615 Å[60]. Table I lists the various material properties obtained at different compressive strains, which we used to compute $\tau_{n\mathbf{k}}$. The unstrained material has a rather low elastic coefficients, but which increases significantly under compressive strain as the interatomic distances shorten. Similarly, the effective ω_{po} increases substantially with strain and reduces the ionic part of the dielectric tensor, with a corresponding reduction in ϵ_s . Deformation potential for select \mathbf{k} -points are given in Supplemental Material Table S1.

TABLE I. Equivalent external pressure, elastic constants, dielectric tensors, and average optical phonon frequency of CsK₂Sb at different amounts of strain.

Strain	0%	1%	2%	3%	4%	5%
Pressure [kB]	0.0	4.46	9.70	15.74	22.69	30.66
C_{11} [GPa]	22.7	25.1	27.8	30.9	34.2	37.8
C_{12} [GPa]	9.8	10.9	12.2	13.7	15.4	17.2
C_{44} [GPa]	13.1	14.6	16.2	18.0	19.8	21.6
ϵ_s	28.1	26.2	23.2	19.2	19.0	16.5
ϵ_∞	7.5	7.6	7.8	7.5	7.6	7.4
ω_{po} [THz]	1.57	1.71	1.87	2.04	2.24	2.44

B. Electronic structure

For unstrained CsK₂Sb, we found a band gap of 1.0 eV with vdW-DF-cx[50] and 1.6 eV with HSE06[54], in good agreement results from previous HSE06 calculations[61] and many-body perturbation theory[62], but somewhat higher than results from experiments[41]. The HSE06 band structure is provided in Supplemental Material Fig. S2. Since the shape of the band structure is very similar with the two functionals, we used vdW-DF-cx to obtain $\varepsilon_{n\mathbf{k}}$ on a dense \mathbf{k} -point grid.

Figure 2 shows the electronic band structure at different strains. For ease of comparison, the band structures are aligned to the Γ point valence band (v) energy $\varepsilon_{v\Gamma}$. The conduction band at zero strain has a Γ -centered minimum with a dispersion similar to a Kane-band, i.e., parabolic-to-linear[64]. Under strain, the conduction band Γ valley shifts upwards while the three-fold degenerate conduction band valley at X remains nearly constant in energy, relative to $\varepsilon_{v\Gamma}$. At a strain of 2%, the two valleys aligns, while for larger strains, the conduction band minimum (CBM) shifts to X.

The valence band between Γ and X has a very flat slope. The band flattens further with increasing compres-

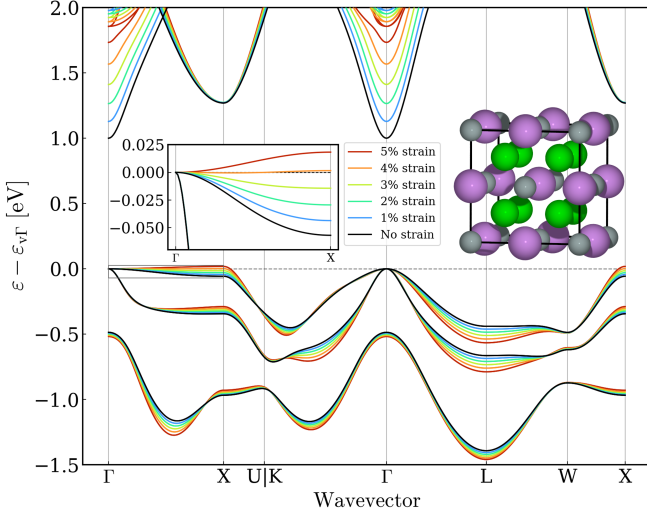


FIG. 2. Electronic band structure at different amounts of compressive strain for CsK₂Sb calculated with the vdW-DF-cx functional. The black lines show the band structure of the equilibrium unit cell. A close-up of the energy dispersion between Γ and X is shown in the inset. The conventional cell of the crystal structure is also shown.

sive strain, i.e., smaller unit cells, and becomes almost constant at 4% strain. Beyond this point, the valence band maximum (VBM) shifts to X. In tandem with the band flattening, the curvature and hence also the electron group velocities, increases perpendicular to this line, as seen by the valence band along the X–U, Γ –L, and X–W lines. Increasing velocities with decreasing volume can be explained by increasing wave function overlaps[65].

Fig. 3 shows energy isosurfaces close to the VBM at different strains and energy values. The 2D-like cylinders result from the almost flat band structure along Γ –X. The flattening of the band structure at 4% strain is reflected in energy isosurface almost extending to three intersecting cylinders even for very small energies below the VBM. The color shades of the isosurfaces, indicating the absolute value of the y -component of the electron velocities $|v_y|$, shows that straining the structure not only enlarges the energy isosurfaces, but also enhance the corresponding effective velocities.

Figure 4 shows the electronic DOS of CsK₂Sb without strain over a wide energy range (a). The near-gap VBM (b) and CBM (c) regions of the DOS are shown at 0%, 2%, and 4% compressive strain. The coloring of the DOS in (b) and (c) are given by the value of running Gaussian average of absolute electron velocity $\langle |v_{n\mathbf{k}}| \rangle$ (see Supplemental Material Eq. S1 for details). The flattening of the valence band makes the sharp increase in the DOS close to the VBM more pronounced. The fact that both the DOS and velocities increased with strain is very distinct from the inherent trade-off between high DOS and velocities in single parabolic band structures[65].

C. Electron transport

Figure 5 shows the Seebeck coefficient S , mobility μ , electrical conductivity σ , electronic thermal conductivity κ_e , power factor (PF), and Lorentz number (L) for p-type CsK₂Sb at 800 K as a function of carrier concentration, for different strains. The predicted μ of the unstrained material is low compared to several common TE materials[66–68], resulting in relatively low σ and κ_e . However, the high DOS allows for high S resulting in a high PF. Our predicted values agree well with those of Yuan et al.[43]. For the doping level of 3.39×10^{20} p/cm³ (corresponding to the optimal carrier concentration N_{opt} for zT , see Fig. 10), $L \approx 1.0 \times 10^{-8}$, which is lower than the value typically used for semiconductors in the non-degenerate limit ($L_0 = 1.5 \times 10^{-8}$ V²/K²)[69, 70]. As more and more effective strategies to reduce κ_e are developed and materials with intrinsic low κ_e are identified, it also becomes more important to identify low L materials alongside a high S at relevant doping concentrations.

Comparing the results for different strains shows that the μ and hence both σ and κ_e of the p-doped material increased. The latter increased somewhat more, so that L increased by 14% to $L = 1.15 \times 10^{-8}$ at 5% strain. Interestingly, there were only small changes to L in the first two percentages of strain. The PF, however, despite only small improvements in S , increased continuously as a function of strain up to an increase of 66% as a result of 5% strain. The resulting zT taking also account of the κ_e (Sec. III E) will be discussed in Sec. III F.

Figure 6 shows the TE properties of the n-type system. The $|S|$ values for the unstrained system is significantly lower than the p-type at their respective relevant doping concentrations. This result can be linked to a CBM at Γ with low effective mass. However, the low effective mass, also makes μ more than an order of magnitude larger than for the p-type. The high μ results in a higher σ and κ_e , and an L that is more than twice that of the p-type material. As strain aligns the Γ and X valleys, with a corresponding increase in DOS, the $|S|$ nearly doubles. As the less dispersive X valley becomes dominant for transport, both σ and κ_e are reduced at a fixed doping concentration, but κ_e falls off faster than σ , greatly reducing L . Despite the reduction in σ for a given carrier concentration, the large increase in $|S|$ dominates and the peak PF still increases up to 2% strain.

D. Electronic scattering

The different scattering rates for CsK₂Sb at selected doping levels are shown for no strain in Fig. 7 (a) and with 2% strain (b). The colored dots indicate the scattering rate $\Gamma_{n\mathbf{k}}$ for the conduction and valence bands for the different scattering mechanisms. It shows that the POP scattering is the dominant scattering mechanism both for p- and n-type, a common feature in polar materials[35, 46, 71–73]. For n-type, the POP scattering

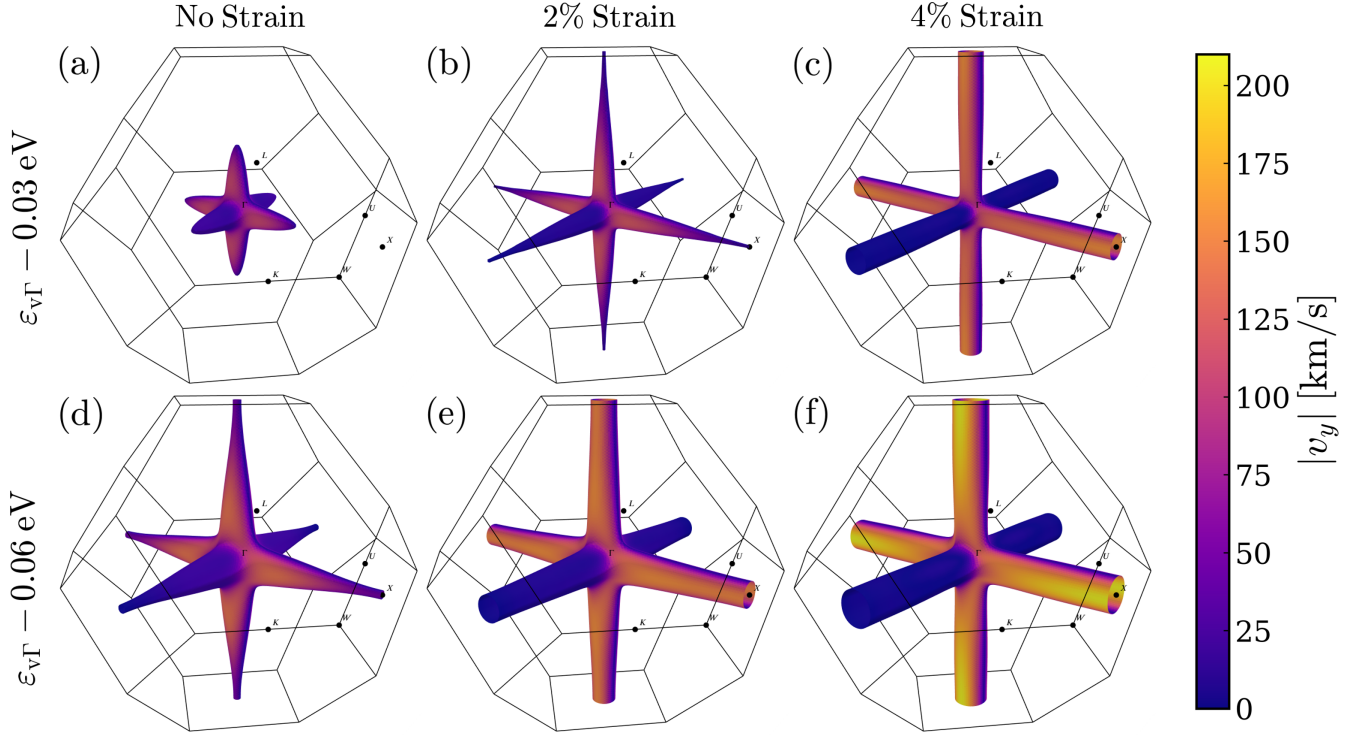


FIG. 3. Energy isosurfaces of CsK₂Sb at 0%, 2%, and 4% compressive strain. The top (bottom) row shows the surfaces at 0.03 eV (0.06 eV) below $\varepsilon_{v\Gamma}$. Colors representing the absolute values of the y -component of the electron velocity are projected onto the surfaces. Surfaces were plotted with IFermi[63].

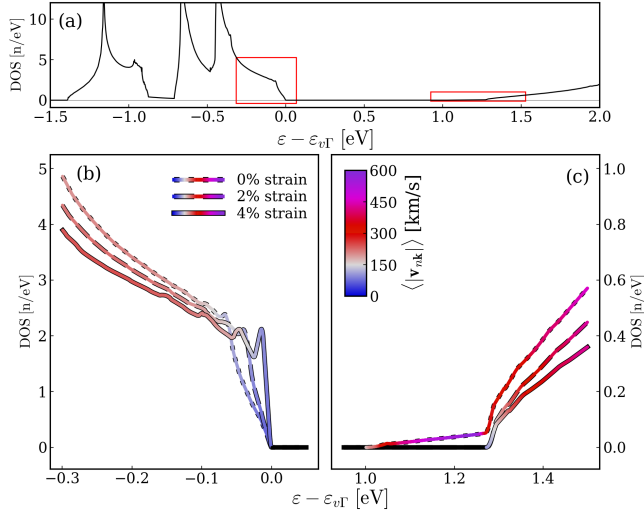


FIG. 4. Density of states (DOS) of CsK₂Sb without strain (a). The red squares mark the close-ups around the VBM (b) and the CBM (c). In (b) and (c), the DOS is given at 0%, 2%, and 4% strain. Each DOS was colored by the moving average absolute velocity $\langle |v_{nk}| \rangle$. When the DOS is zero, the color is black.

rates of the Γ valley are lower than p-type, while for the X valley the scattering rates are almost equal. IMP scattering is also important for low-energetic carriers, while

ADP is more important than IMP for p-type and less important for n-type. The total scattering rates for most of the p- and n-type states are almost the same magnitude, especially at 2% strain where the higher scattering rate X valley contributes more. With the same material parameters for n- and p-type (used in Eq. A1-A6), scattering rates could be expected to mostly depend on the effective scattering spaces, according to the commonly used $\tau \propto \frac{1}{\text{DOS}}$ -approximation[74–76].

The fact that the highly differing n and p-type DOS do not have a greater impact on the scattering rates can be understood by considering the \mathbf{q} -dependence of the individual scattering mechanisms. For the dominant POP scattering, the $\propto \frac{1}{q^2}$ factor results in reduced scattering between the different cylinders of the Fermi surface due to the large distance in \mathbf{k} -space. For the long-ranged ADP scattering, lacking this factor, the p-type ADP scattering is an order of magnitude larger than the n-type. Finally, for the short-ranged ($\propto \frac{1}{q^4}$) IMP scattering, both the n- and p-type materials scatters the most close to their respective band minimum or maximum. Further away from the band edge, the scattering rates quickly falls off due to the longer distances within the Fermi surface. It should be noted that the n- and p-type scattering rates are shown for different carrier concentrations, each at their respective N_{opt} . Higher carrier concentration tends to decrease POP scattering due to free-carrier screening, while the high doping increases the number of ionized

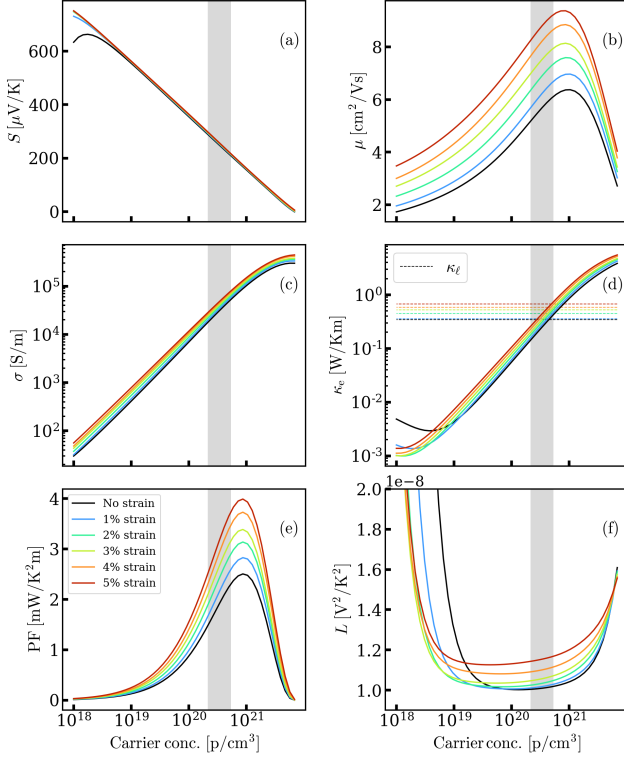


FIG. 5. Electron transport properties: The Seebeck coefficient S (a), mobility μ (b), electronic conductivity σ (c), electronic part of the thermal conductivity κ_e (d), power factor PF (e), and Lorentz number L (f) at 800 K for p-type CsK₂Sb at varying compressive strain. The grey area indicates the carrier concentration region around maximum zT .

impurities and thereby IMP scattering.

With more realistic scattering models like in AMSET, the relaxation time depends on the band and the \mathbf{k} -point and thus generally have a wide spread of values. To assist in the interpretation of the magnitude of different scattering mechanisms, we introduce an effective relaxation time τ_{eff} , which is defined as the CRTA value that reproduces the same σ as the AMSET distribution of $\tau_{n\mathbf{k}}$ for a given T and carrier concentration.

Figure 8 shows τ_{eff} for different scattering mechanisms with varying strain and doping concentrations. Each "bundle" of lines represents the τ_{eff} depending on a specific scattering mechanism, or the total scattering rate, at different levels of strain. At low doping, $\tau_{\text{eff}}^{\text{TOT}}$ is almost entirely limited by POP scattering. With increasing doping, the free carriers reduces the POP scattering. Simultaneously, increased doping also increases the ionized impurity scattering, making it the dominant scattering mechanism at high carrier concentrations. ADP scattering is independent of carrier concentration and $\tau_{\text{eff}}^{\text{ADP}}$ only changes at very high carrier concentrations due to the shift in Fermi level this doping represents.

The effect of strain on the different scattering mechanisms can be linked to the changing material properties

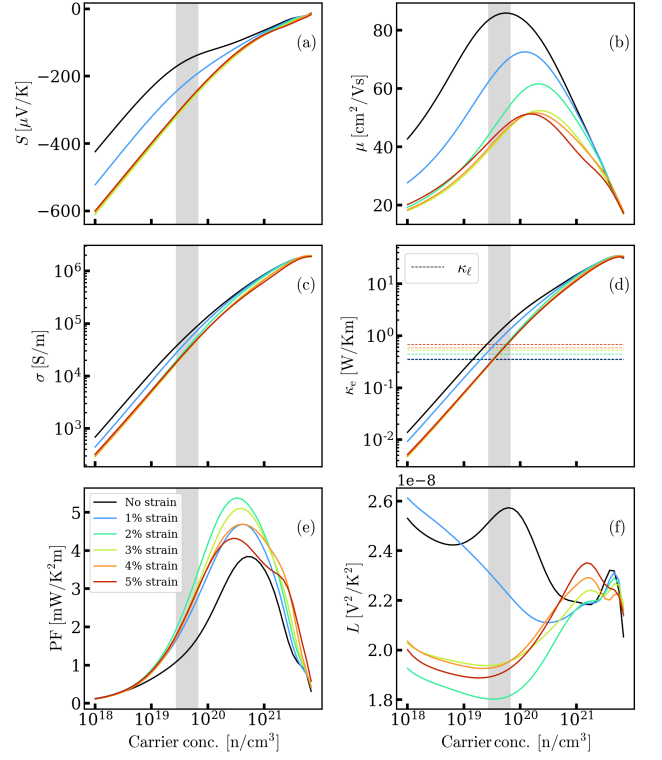


FIG. 6. Electron transport properties: (a) S , (b) μ , (d) σ , (d) κ_e , (e) PF, and (f) L at 800 K for n-doped CsK₂Sb at varying levels of strain.

listed in Table I. Under compressive strain, with a reduction in the ionic contribution to the static dielectric tensor, the POP scattering decreases. Simultaneously, the IMP scattering increases due to the reduction in ϵ_s . For ADP, the major change in scattering rates is due to the changes to the elastic constants and the resulting changes to the sound velocity in Eq. A1. The net effect on $\tau_{\text{eff}}^{\text{TOT}}$, at N_{opt} , is an increase of 10% when going from 0 to 5% strain. As this is much less than the increase in mobility, the effect of the changing band curvature must be substantial.

Figure 8 shows the conduction band τ_{eff} as a function of carrier concentration at varying strain. The general trends of τ_{eff} are similar to those of the valence band but with some notable differences. Primarily, these differences stems from the two conduction band valleys (Γ and X) contributing with different scattering rates, see Fig. 7. Since the Fermi level is determined by doping and strain changes the relative energy minimum of the two valleys, both of these parameters changes the relative contribution of the two valleys to τ_{eff} . For POP scattering at low carrier concentration, increasing strain decreases τ_{eff} as the X-valley becomes the major contributor to transport and had higher scattering rates, see Fig. 7. At high doping, both valleys contribute to the expected change in $\tau_{\text{eff}}^{\text{POP}}$, seen for p-type, when strain is introduced.

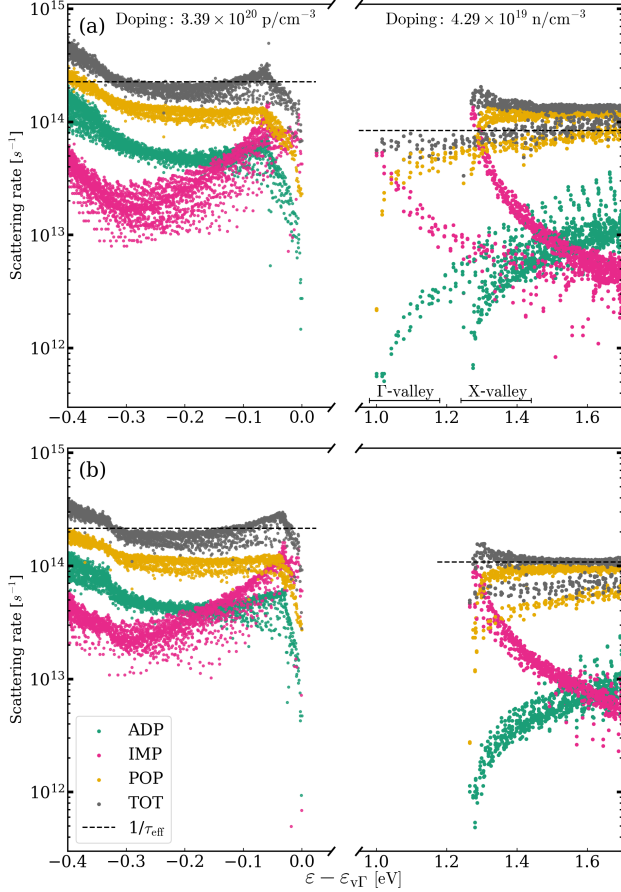


FIG. 7. Scattering rates $\Gamma_{n\mathbf{k}}$ of ADP, IMP, POP, and total scattering shown for the valence band and conduction band of unstrained CsK_2Sb at 800 K for (a) 0% strain and (b) 2% strain. For the conduction band at 0% strain, the lowest 0.2 eV of the Γ -valley and X-valley are indicated.

For $\tau_{\text{eff}}^{\text{ADP}}$, we observe something similar, but only up to 2% strain. For ADP, the two valleys has similar scattering rates that increased with carrier concentration. At a given carrier concentration; however, the effective carrier concentration per band is reduced as the band aligns, resulting in reduced $\tau_{\text{eff}}^{\text{ADP}}$. As $\tau_{\text{eff}}^{\text{TOT}}$ is almost entirely dominated by POP scattering at N_{opt} , the changes to $\tau_{\text{eff}}^{\text{TOT}}$ under strain closely resembled the changes to $\tau_{\text{eff}}^{\text{POP}}$.

While lifetimes were substantially shorter for p-doped, at optimal doping, the n-type optimum is quite similar to the conventional choice of $\tau = 10^{-14}$ s.

E. Lattice thermal conductivity

The calculated phonon properties of CsK_2Sb are shown in Fig. 9. The phonon dispersion relation for $T = 300$ K is given in Fig. 9(a) with a compressive strain varying from 0 to 5% (see legend in Fig. 9(b).) It is seen how the phonon frequencies increased as the unit cell was compressed.

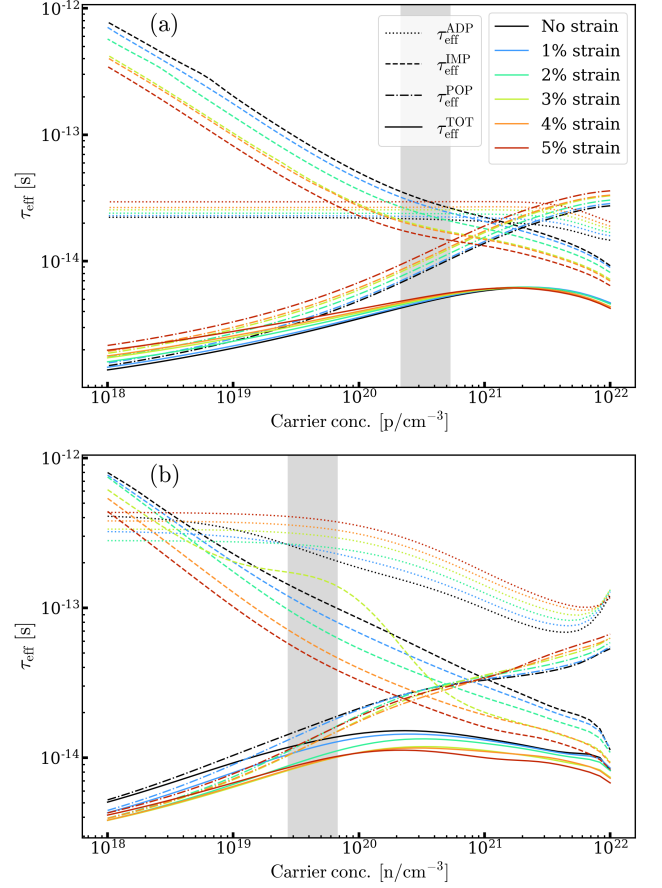


FIG. 8. Effective relaxation time τ_{eff} of the valence band at carrier concentrations and different strains at a temperature of 800 K for (a) p-type and (b) n-type. Plots are shown for relaxation times due to single scattering mechanism as well as that of the total effective scattering rate $\tau_{\text{eff}}^{\text{TOT}}$.

The resulting κ_{ℓ} is shown in Fig. 9(b). The predicted lattice thermal conductivity of the unstrained structure was $\kappa_{\ell} = 0.91 \text{ Wm}^{-1}\text{K}^{-1}$ at 300 K, going down to $0.35 \text{ Wm}^{-1}\text{K}^{-1}$ at 800 K. Although the predicted κ_{ℓ} values were low, they are 3–6 times higher than previous predictions, [43, 45], possibly due to the highly anharmonic effect captured by previous studies using molecular dynamics-based κ_{ℓ} evaluation. κ_{ℓ} increased with increasing compressive strain, except when going from no strain to 1 % strain, for which there was virtually no change in κ_{ℓ} .

This behavior can be understood from the cumulative and spectral κ_{ℓ} (Fig. 9(c) and (d)). Looking at the contribution from phonons with varying MFP (c), the ones with the lowest MFP contributed less to the total κ_{ℓ} when compressive strain was applied, while the opposite was the case for high MFPs. The case with 1% strain stands out, where the highest MFP phonons contributed less than those of the strain-free material. [77] Turning to the spectral κ_{ℓ} (d), strain reduced the contributions to κ_{ℓ} from phonons with low frequency (< 0.5 THz), while

contributions from the regions around 1 and 2 THz increased. At 1%, the reduction at low frequencies almost canceled the increase at higher frequencies, while there was a significant net increase for larger strains.

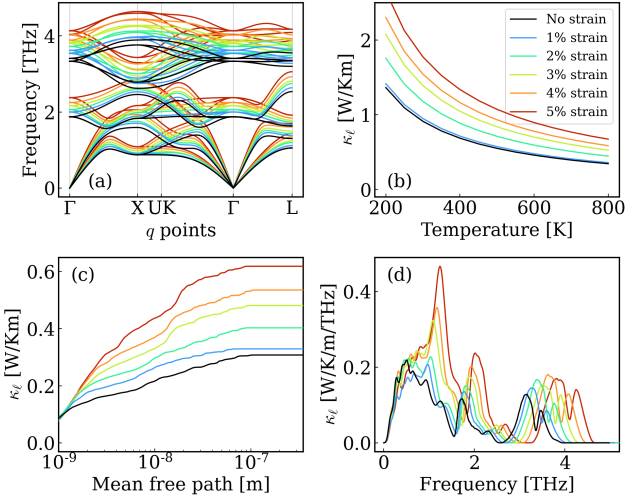


FIG. 9. Phonon properties of CsK₂Sb at different compressive strains calculated with TDEP: (a) Phonon dispersion relation, (b) κ_L as a function of temperature, (c) cumulative κ_L as a function of the mean free path (MFP) ($T = 800$ K), (d) spectral κ_L as a function of the phonon frequency ($T = 800$ K).

F. Figure of merit

Figure 10(a) and (b) show zT as a function of carrier concentration for p- and n-type CsK₂Sb at 800 K. For the unstrained p-type material, the high PF combined with the low $\kappa = \kappa_e + \kappa_L$ resulted in a zT of 2.6 at a carrier concentration of 3.39×10^{20} p/cm³. As the material was strained, flattening the valence band and increasing velocities, the PF increased more than κ , resulting in a maximum zT of 2.7 at 1% strain. After this, the increase in κ_L dominated and further strain only served to reduce the maximum zT .

For n-type, the low S and relatively high κ_e resulting from the low DOS gave a zT of 0.8 at 800 K. With the alignment of the Γ and X valleys under strain, a simultaneous increase of S and decrease of κ_e led to a large increase of the PF and the zT . With 1% strain resulting in a zT of 1.5, and 2% strain resulting in $zT = 2.3$, an almost three-fold increase from the unstrained structure could be observed. Further strain removed the valley alignment, thus decreasing the power factor. The accompanying increase in κ_L decreased zT .

Figure 10(c) and (d) show the maximal p- and n-type zT as a function of T for each strain. While only moderate changes can be seen with strain, the p-type material can achieve a zT of 1 below 400 K. For the n-type mate-

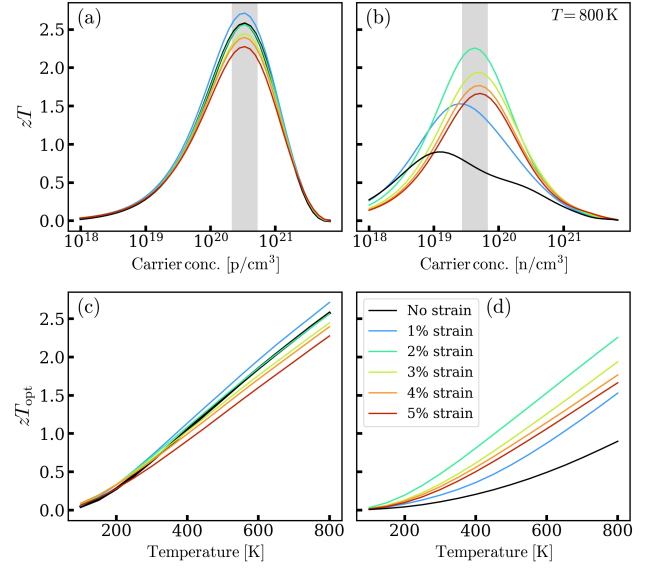


FIG. 10. zT of (a) p-type and (b) n-type doped CsK₂Sb at 800 K at varying strain. (c) and (d) show the charge carrier-optimized zT at different temperatures for p- and n-type, respectively.

rial, the optimal strain of 2% resulted in a large increase in zT at all temperatures, with zT reaching just below 1 at 400 K.

IV. DISCUSSION

TE materials with low-dimensional Fermi surfaces are attractive due to their high DOS which allows S to be high at high carrier concentrations. A high DOS, however, gives many allowed scattering processes, which may increase scattering rates and thereby reduce μ . Comparing the scattering rates of n- and p-type CsK₂Sb can elucidate the role of DOS, since their scattering prefactors are quite similar but the valence band has a much larger DOS than the conduction band. In the case of ADP scattering, this difference results in an order of magnitude larger scattering rates for p-type than for n-type. On the other hand, this difference is reduced to about a factor of 4 (2) for IMP (POP) scattering. The reduced DOS sensitivity can be explained by the \mathbf{q} -dependence of these scattering rates. Since POP often has the largest scattering rate, this result is very encouraging for TE materials with low dimensional band structures since they extend over large parts of the Brillouin zone.

There is an interesting trade-off in the effect of strain on κ_L and τ_{eff} related to the material parameters in Tab. I entering into the scattering coefficients. Reducing the volume increases elastic constants and thus ADP scattering through the reduced sound velocity, c (Eq. A1). Further, the ionic contribution to the dielectric tensor is reduced, thereby reducing POP scattering, but it also

increases IMP scattering, see Eqs. A4,A2. In most materials, an increase in elastic constants under compressive strain will also increase κ_ℓ [78–81], though exceptions do exist[79, 80, 82]. This inverse relationship between κ_ℓ and τ could be expected in other materials as well, where POP or ADP are the dominant scattering mechanisms.

The optimal p-type carrier concentrations, i.e. $\sim 10^{20}$ e/cm⁻³ is more than an order of magnitude larger than that of the n-type, which should also be the case for other materials with low-dimensional electronic band structures[22, 24, 26]. Recently, Lou et al. [83] argued that this could be an attractive feature as low optimal doping values are more vulnerable to doping variations such as intrinsic doping and impurities, which can increase the cost of synthesis and raw materials. On the other hand, high doping also requires high dopability. The fact that a high zT can be achieved, at finite strain, for both p- and n-type is technologically attractive since thermomechanical properties would be similar, and the same metallization schemes and bonding materials might be used for both contacts.

The hydrostatic stress needed to reach the larger strain values studied here is unrealistic in practical devices. In practice, one would need "chemical" pressure, i.e. alloying with smaller, isovalent elements[81]. However, such isovalent substitution might also introduce significant changes to the band structure and material properties. Critically, it would also introduce additional electronic carrier scattering mechanisms. The overall effect might still be beneficial, as isovalent alloying can further decrease κ_ℓ [5, 84, 85].

CsK₂Sb is not the only material to display a low-dimensional band structure. Examples of low-dimensional band structures similar to CsK₂Sb include Rb₂CsSb[42], KCs₂Sb, CsK₂Bi, and CsK₂As[86], and compounds in the A₃Sb class, Cs₃Sb [38], Na₃Sb [37], and K₃Sb [38, 39]. Many of the A₃Sb compounds without low-dimensional band structures have also been predicted to exhibit excellent TE properties due to their ultra-low κ_ℓ . A promising path forward could be to investigate the miscibility of the solid solutions of these compounds, which could provide the desired chemical pressure. This could give access to a continuous range of band structures and scattering mechanisms, providing good prospects for designing materials with outstanding TE properties.

V. CONCLUSION AND OUTLOOK

The thermoelectric properties of CsK₂Sb were in this study investigated with electron transport based on momentum-resolved scattering in AMSET and phonon properties with TDEP. For p-doped CsK₂Sb we showed that low-dimensional band structures lead to promising thermoelectric materials because of the combination of high electronic DOS near the Fermi level and high electron velocities. Crucially, when moving beyond the CRTA and including momentum-dependent electron

scattering, we found that the long distance between states in **k**-space results in low polar optical phonon and ionized impurity scattering rates; significantly lower than what would generally be expected with such a high DOS. Similar results could be expected in other materials with low-dimensional band structure where **q**-dependent POP or IMP scattering dominates. These results highlight the importance of moving beyond the CRTA to correctly identify materials with a high potential as TE materials.

When strain was added to the structure, the electronic transport properties changed significantly. For the p-doped material, the ideal Fermi surfaces could be optimized towards highly pronounced low-dimensionality at around 2% compressive strain, which led to a significant increase of the power factor. The n-doped material had an even higher increase, due to valley alignment of the electronic band structure. This was partially counteracted by the lattice thermal conductivity, which increased when strain was added. Nevertheless, the strain-optimized p- and n-doped materials showed very promising TE properties, with a maximal figure of merit at 800 K of 2.7 and 2.3, respectively.

We believe that CsK₂Sb with repeatedly predicted superior TE properties merits further investigation, as do related antimonides rich on alkali metals. Further *ab initio* calculations to explore the n- and p-type dopability and identify proper candidates for solid solutions should be performed. More advanced methods for determining the band structure and transport properties should also be employed. Ultimately, targeted synthesis and characterization to experimentally verify TE properties is needed.

ACKNOWLEDGMENTS

The computations in this work were funded by The Norwegian e-infrastructure for research and education, Sigma2, through grants No. nn9711k and nn2615k. Ø.A.G., O.M.L, and K.B. gratefully acknowledge funding by the Research Council of Norway through the Allotherm project (Project No. 314778) and G.J.S. by the Humboldt Foundation.

Appendix A: Scattering matrix elements

In AMSET[46], the matrix elements between state $|n\mathbf{k}\rangle$ and $\langle m\mathbf{k}+\mathbf{q}|$ for acoustic deformation potential scattering are calculated as

$$g_{nm}^{\text{adp}} = \sqrt{k_B T} \sum_{\mathbf{G} \neq -\mathbf{q}} \left[\frac{\tilde{\mathbf{D}}_{n\mathbf{k}} : \hat{\mathbf{S}}_l}{c_l \sqrt{\rho}} + \frac{\tilde{\mathbf{D}}_{n\mathbf{k}} : \hat{\mathbf{S}}_{t_1}}{c_{t_1} \sqrt{\rho}} + \frac{\tilde{\mathbf{D}}_{n\mathbf{k}} : \hat{\mathbf{S}}_{t_2}}{c_{t_2} \sqrt{\rho}} \right] \times \langle m\mathbf{k} + \mathbf{q} | e^{i(\mathbf{q}+\mathbf{G}) \cdot \mathbf{r}} | n\mathbf{k} \rangle, \quad (\text{A1})$$

where $\tilde{\mathbf{D}}_{n\mathbf{k}}$ is the velocity-adjusted deformation potential $\mathbf{D}_{n\mathbf{k}} + \mathbf{v}_{n\mathbf{k}} \otimes \mathbf{v}_{n\mathbf{k}}$, ρ is the density, $\hat{\mathbf{S}}$ is unit strain, and c

is the velocity of sound. The subscripts l , $t1$, and $t2$ denotes the one longitudinal and two transverse directions, respectively.

The ionized impurity scattering matrix elements are given by

$$g_{nm}^{\text{imp}} = \sum_{\mathbf{G} \neq -\mathbf{q}} \frac{n_{ii}^{1/2} Z e}{\hat{\mathbf{n}} \cdot \boldsymbol{\epsilon}_s \cdot \hat{\mathbf{n}}} \frac{\langle m\mathbf{k} + \mathbf{q} | e^{i(\mathbf{q}+\mathbf{G}) \cdot \mathbf{r}} | n\mathbf{k} \rangle}{|\mathbf{q} + \mathbf{G}|^2 + \beta_s^2}, \quad (\text{A2})$$

where $n_{ii} = (n_h - n_e)/Z$ is the ionized impurity concentration, Z is the unscreened charge of the impurity, and e is the electron charge. β_s is the inverse screening length, given as

$$\beta_s^2 = \frac{e^2}{\epsilon_s k_B T} \int \frac{d\varepsilon}{V} D(\varepsilon) f(\varepsilon) (1 - f(\varepsilon)) \quad (\text{A3})$$

where ϵ_s is the static dielectric tensor, V is the unit cell volume, D is the DOS, and f is the Fermi-Dirac distribution function.

The polar optical phonon scattering matrix element is

given by

$$g_{nm}^{\text{pop}} = \left[\frac{\hbar \omega_{po}}{2} \right]^{1/2} \sum_{\mathbf{G} \neq -\mathbf{q}} \left(\frac{1}{\hat{\mathbf{n}} \cdot \boldsymbol{\epsilon}_\infty \cdot \hat{\mathbf{n}}} - \frac{1}{\hat{\mathbf{n}} \cdot \boldsymbol{\epsilon}_s \cdot \hat{\mathbf{n}}} \right)^{1/2} \times \frac{\langle m\mathbf{k} + \mathbf{q} | e^{i(\mathbf{q}+\mathbf{G}) \cdot \mathbf{r}} | n\mathbf{k} \rangle}{|\mathbf{q} + \mathbf{G}| + \beta_\infty}, \quad (\text{A4})$$

where $\hat{\mathbf{n}}$ is the normalized vector of scattering, ϵ_∞ is the high frequency and ϵ_s , the static dielectric tensors. An effective optical phonon frequency is obtained by the weighted average of the phonon frequencies ω_{po} ,

$$\omega_{po} = \frac{\sum_\nu \omega_{\Gamma\nu} w_\nu}{\sum_\nu w_\nu}. \quad (\text{A5})$$

Here, $\omega_{\Gamma\nu}$ is the frequency of phonon branch ν at the Γ -point and the weight is defined as

$$w_\nu = \sum_\alpha \left[\frac{1}{M_\alpha \omega_{\mathbf{q}\nu}} \right]^{1/2} \times [\mathbf{q} \cdot \mathbf{Z}_\alpha^* \cdot \mathbf{e}_{\alpha\nu}], \quad (\text{A6})$$

where M is atomic mass, \mathbf{Z}_α^* is Born effective charge, $\mathbf{e}_{\alpha\nu}$ is a phonon eigenvector, and the index α runs over the atoms of the unit cell.

-
- [1] G. J. Snyder and E. S. Toberer, Complex thermoelectric materials, *Nature Materials* **7**, 105 (2008).
 - [2] C. B. Vining, An inconvenient truth about thermoelectrics, *Nature Materials* **8**, 83 (2009).
 - [3] J. Schwab, M. Bernecker, S. Fischer, B. Seyed Sadjjadi, M. Kober, F. Rinderknecht, and T. Siefkes, Exergy Analysis of the Prevailing Residential Heating System and Derivation of Future CO2-Reduction Potential, *Energies* **15**, 3502 (2022).
 - [4] L. E. Bell, Cooling, Heating, Generating Power, and Recovering Waste Heat with Thermoelectric Systems, *Science* **321**, 1457 (2008).
 - [5] R. Tranås, O. M. Løvrvik, and K. Berland, Attaining Low Lattice Thermal Conductivity in Half-Heusler Sublattice Solid Solutions: Which Substitution Site Is Most Effective?, *Electronic Materials* **3**, 1 (2022).
 - [6] A. J. Minnich, M. S. Dresselhaus, Z. F. Ren, and G. Chen, Bulk nanostructured thermoelectric materials: Current research and future prospects, *Energy & Environmental Science* **2**, 466 (2009).
 - [7] J. Zhang, L. Song, G. K. H. Madsen, K. F. F. Fischer, W. Zhang, X. Shi, and B. B. Iversen, Designing high-performance layered thermoelectric materials through orbital engineering, *Nature Communications* **7**, 10892 (2016).
 - [8] J. Li, S. Zhang, B. Wang, S. Liu, L. Yue, G. Lu, and S. Zheng, Designing high-performance n-type Mg_3Sb_2 -based thermoelectric materials through forming solid solutions and biaxial strain, *Journal of Materials Chemistry A* **6**, 20454 (2018).
 - [9] Y. Pei, X. Shi, A. LaLonde, H. Wang, L. Chen, and G. J. Snyder, Convergence of electronic bands for high performance bulk thermoelectrics, *Nature* **473**, 66 (2011).
 - [10] Y. Zhu, D. Wang, T. Hong, L. Hu, T. Ina, S. Zhan, B. Qin, H. Shi, L. Su, X. Gao, and L.-D. Zhao, Multiple valence bands convergence and strong phonon scattering lead to high thermoelectric performance in p-type PbSe, *Nature Communications* **13**, 4179 (2022).
 - [11] D. Bilec, S. D. Mahanti, E. Quarez, K.-F. Hsu, R. Pcionek, and M. G. Kanatzidis, Resonant States in the Electronic Structure of the High Performance Thermoelectrics $\text{AgPb}_{10}\text{Sb}_{14}\text{Te}_{22}$: The Role of Ag-Sb Microstructures, *Physical Review Letters* **93**, 146403 (2004).
 - [12] J. P. Heremans, V. Jovovic, E. S. Toberer, A. Samarat, K. Kurosaki, A. Charoenphakdee, S. Yamanaka, and G. J. Snyder, Enhancement of Thermoelectric Efficiency in PbTe by Distortion of the Electronic Density of States, *Science* **321**, 554 (2008).
 - [13] J. P. Heremans, B. Wiendlocha, and A. M. Chamoire, Resonant levels in bulk thermoelectric semiconductors, *Energy Environ. Sci.* **5**, 5510 (2012).
 - [14] S. V. Faleev and F. Léonard, Theory of enhancement of thermoelectric properties of materials with nanoinclusions, *Physical Review B* **77**, 214304 (2008).
 - [15] C. Gayner and Y. Amouyal, Energy Filtering of Charge Carriers: Current Trends, Challenges, and Prospects for Thermoelectric Materials, *Advanced Functional Materials* **30**, 1901789 (2020).
 - [16] Y. Lin, M. Wood, K. Imasato, J. J. Kuo, D. Lam, A. N. Mortazavi, T. J. Slade, S. A. Hodge, K. Xi, M. G. Kanatzidis, D. R. Clarke, M. C. Hersam, and G. J. Snyder, Expression of interfacial Seebeck coefficient through grain boundary engineering with multi-layer graphene nanoplatelets, *Energy & Environmental Science* **13**, 4114

- (2020).
- [17] L. D. Hicks and M. S. Dresselhaus, Effect of quantum-well structures on the thermoelectric figure of merit, *Physical Review B* **47**, 12727 (1993).
 - [18] L. D. Hicks and M. S. Dresselhaus, Thermoelectric figure of merit of a one-dimensional conductor, *Physical Review B* **47**, 16631 (1993).
 - [19] J. E. Cornett and O. Rabin, Thermoelectric figure of merit calculations for semiconducting nanowires, *Applied Physics Letters* **98**, 182104 (2011).
 - [20] J. E. Cornett and O. Rabin, Universal scaling relations for the thermoelectric power factor of semiconducting nanostructures, *Physical Review B* **84**, 205410 (2011).
 - [21] L. Yang, Z.-G. Chen, M. S. Dargusch, and J. Zou, High Performance Thermoelectric Materials: Progress and Their Applications, *Advanced Energy Materials* **8**, 1701797 (2018).
 - [22] D. Parker, X. Chen, and D. J. Singh, High Three-Dimensional Thermoelectric Performance from Low-Dimensional Bands, *Physical Review Letters* **110**, 146601 (2013).
 - [23] D. I. Bilc, G. Hautier, D. Waroquiers, G.-M. Rignanese, and P. Ghosez, Low-Dimensional Transport and Large Thermoelectric Power Factors in Bulk Semiconductors by Band Engineering of Highly Directional Electronic States, *Physical Review Letters* **114**, 136601 (2015).
 - [24] M. T. Dylla, S. D. Kang, and G. J. Snyder, Effect of Two-Dimensional Crystal Orbitals on Fermi Surfaces and Electron Transport in Three-Dimensional Perovskite Oxides, *Angewandte Chemie International Edition* **58**, 5503 (2019).
 - [25] J. Park, Y. Xia, V. Ozoliņš, and A. Jain, Optimal band structure for thermoelectrics with realistic scattering and bands, *npj Computational Materials* **7**, 43 (2021).
 - [26] M. K. Brod and G. J. Snyder, Orbital chemistry of high valence band convergence and low-dimensional topology in PbTe, *Journal of Materials Chemistry A* **9**, 12119 (2021).
 - [27] G. K. H. Madsen, Automated Search for New Thermoelectric Materials: The Case of LiZnSb, *Journal of the American Chemical Society* **128**, 12140 (2006).
 - [28] S. Wang, Z. Wang, W. Setyawan, N. Mingo, and S. Curtarolo, Assessing the Thermoelectric Properties of Sintered Compounds via High-Throughput *Ab-Initio* Calculations, *Physical Review X* **1**, 021012 (2011).
 - [29] S. Bhattacharya and G. K. H. Madsen, High-throughput exploration of alloying as design strategy for thermoelectrics, *Physical Review B* **92**, 085205 (2015).
 - [30] F. Ricci, W. Chen, U. Aydemir, G. J. Snyder, G.-M. Rignanese, A. Jain, and G. Hautier, An *ab initio* electronic transport database for inorganic materials, *Scientific Data* **4**, 170085 (2017).
 - [31] K. Berland, N. Shulumba, O. Hellman, C. Persson, and O. M. Løvvik, Thermoelectric transport trends in group 4 half-Heusler alloys, *Journal of Applied Physics* **126**, 145102 (2019).
 - [32] K. Berland, O. M. Løvvik, and R. Tranås, Discarded gems: Thermoelectric performance of materials with band gap emerging at the hybrid-functional level, *Applied Physics Letters* **119**, 081902 (2021).
 - [33] J. Park, Y. Xia, and V. Ozoliņš, High Thermoelectric Power Factor and Efficiency from a Highly Dispersive Band in Ba₂BiAu, *Physical Review Applied* **11**, 014058 (2019).
 - [34] J. Park, M. Dylla, Y. Xia, M. Wood, G. J. Snyder, and A. Jain, When band convergence is not beneficial for thermoelectrics, *Nature Communications* **12**, 3425 (2021).
 - [35] Z. Li, P. Graziosi, and N. Neophytou, Efficient first-principles electronic transport approach to complex band structure materials: The case of n-type Mg₃Sb₂, *npj Computational Materials* **10**, 8 (2024).
 - [36] J. Ji, Q. Tang, M. Yao, H. Yang, Y. Jin, Y. Zhang, J. Xi, D. J. Singh, J. Yang, and W. Zhang, Functional-Unit-Based Material Design: Ultralow Thermal Conductivity in Thermoelectrics with Linear Triatomic Resonant Bonds, *Journal of the American Chemical Society* **144**, 18552 (2022).
 - [37] A. R. H. F. Ettema and R. A. De Groot, Electronic structure of Na₃Sb and Na₂KSb, *Physical Review B* **61**, 10035 (2000).
 - [38] L. Kalarasse, B. Bennecer, F. Kalarasse, and S. Djeroud, Pressure effect on the electronic and optical properties of the alkali antimonide semiconductors Cs₃Sb, KCs₂Sb, CsK₂Sb and K₃Sb: *Ab initio* study, *Journal of Physics and Chemistry of Solids* **71**, 1732 (2010).
 - [39] P. Liu, Y. Zhao, J. Ni, and Z. Dai, Influence of anharmonicity on the thermoelectric properties of alkali antimonide compounds M₃Sb (M = Na, K, Rb, Cs), *Physical Review Applied* **22**, 034049 (2024).
 - [40] A. H. Sommer, A NEW ALKALI ANTIMONIDE PHOTOEMITTER WITH HIGH SENSITIVITY TO VISIBLE LIGHT, *Applied Physics Letters* **3**, 62 (1963).
 - [41] C. Ghosh and B. P. Varma, Preparation and study of properties of a few alkali antimonide photocathodes, *Journal of Applied Physics* **49**, 4549 (1978).
 - [42] T. Yue, P. Sui, Y. Zhao, J. Ni, S. Meng, and Z. Dai, Theoretical prediction of mechanics, transport, and thermoelectric properties of full Heusler compounds Na₂KSb and X₂CsSb (X = K, Rb), *Physical Review B* **105**, 184304 (2022).
 - [43] K. Yuan, X. Zhang, Z. Chang, D. Tang, and M. Hu, Antibonding induced anharmonicity leading to ultralow lattice thermal conductivity and extraordinary thermoelectric performance in CsK₂X (X = Sb, Bi), *Journal of Materials Chemistry C* **10**, 15822 (2022).
 - [44] U. Singh, S. Singh, M. Zeeshan, J. Van Den Brink, and H. C. Kandpal, Low lattice thermal conductivity in alkali metal based Heusler alloys, *Physical Review Materials* **6**, 125401 (2022).
 - [45] G. Sharma, M. Sajjad, and N. Singh, Impressive Electronic and Thermal Transports in CsK₂Sb: A Thermoelectric Perspective, *ACS Applied Energy Materials* **6**, 11179 (2023).
 - [46] A. M. Ganose, J. Park, A. Faghaninia, R. Woods-Robinson, K. A. Persson, and A. Jain, Efficient calculation of carrier scattering rates from first principles, *Nature Communications* **12**, 2222 (2021).
 - [47] G. K. Madsen, J. Carrete, and M. J. Verstraete, BoltzTraP2, a program for interpolating band structures and calculating semi-classical transport coefficients, *Computer Physics Communications* **231**, 140 (2018).
 - [48] G. Kresse and J. Hafner, *Ab Initio* molecular dynamics for liquid metals, *Physical Review B* **47**, 558 (1993).
 - [49] G. Kresse and D. Joubert, From ultrasoft pseudopotentials to the projector augmented-wave method, *Physical Review B* **59**, 1758 (1999).
 - [50] K. Berland and P. Hyldgaard, Exchange functional that

- tests the robustness of the plasmon description of the van der Waals density functional, *Physical Review B* **89**, 035412 (2014).
- [51] K. Berland, C. A. Arter, V. R. Cooper, K. Lee, B. I. Lundqvist, E. Schröder, T. Thonhauser, and P. Hyldgaard, Van der Waals density functionals built upon the electron-gas tradition: Facing the challenge of competing interactions, *The Journal of Chemical Physics* **140**, 18A539 (2014).
 - [52] T. Björkman, Testing several recent van der Waals density functionals for layered structures, *The Journal of Chemical Physics* **141**, 074708 (2014).
 - [53] F. Tran, L. Kalantari, B. Traoré, X. Rocquefelte, and P. Blaha, Nonlocal van der Waals functionals for solids: Choosing an appropriate one, *Physical Review Materials* **3**, 063602 (2019).
 - [54] A. V. Krukau, O. A. Vydrov, A. F. Izmaylov, and G. E. Scuseria, Influence of the exchange screening parameter on the performance of screened hybrid functionals, *The Journal of Chemical Physics* **125**, 224106 (2006).
 - [55] A. Jain, S. P. Ong, G. Hautier, W. Chen, W. D. Richards, S. Dacek, S. Cholia, D. Gunter, D. Skinner, G. Ceder, and K. A. Persson, Commentary: The Materials Project: A materials genome approach to accelerating materials innovation, *APL Materials* **1**, 011002 (2013).
 - [56] M. Gajdoš, K. Hummer, G. Kresse, J. Furthmüller, and F. Bechstedt, Linear optical properties in the projector-augmented wave methodology, *Physical Review B* **73**, 045112 (2006).
 - [57] Y. Le Page and P. Saxe, Symmetry-general least-squares extraction of elastic data for strained materials from *ab initio* calculations of stress, *Physical Review B* **65**, 104104 (2002).
 - [58] N. Shulumba, O. Hellman, and A. J. Minnich, Intrinsic localized mode and low thermal conductivity of PbSe, *Physical Review B* **95**, 014302 (2017).
 - [59] F. Knoop, N. Shulumba, A. Castellano, J. P. A. Batista, R. Farris, M. J. Verstraete, M. Heine, D. Broido, D. S. Kim, J. Klarbring, I. A. Abrikosov, S. I. Simak, and O. Hellman, TDEP: Temperature Dependent Effective-Potentials, *Journal of Open Source Software* **9**, 6150 (2024).
 - [60] W. McCarroll, Chemical and structural characteristics of the potassium-cesium-antimony photocathode, *Journal of Physics and Chemistry of Solids* **26**, 191 (1965).
 - [61] R. Wu and A. M. Ganose, Relativistic electronic structure and photovoltaic performance of K_2 CsSb, *Journal of Materials Chemistry A* **11**, 21636 (2023).
 - [62] C. Cocchi, S. Mistry, M. Schmeißer, J. Kühn, and T. Kamps, First-principles many-body study of the electronic and optical properties of CsK₂ Sb, a semiconducting material for ultra-bright electron sources, *Journal of Physics: Condensed Matter* **31**, 014002 (2019).
 - [63] A. Ganose, A. Searle, A. Jain, and S. Griffin, IFermi: A python library for Fermi surface generation and analysis, *Journal of Open Source Software* **6**, 3089 (2021).
 - [64] E. O. Kane, Band structure of indium antimonide, *Journal of Physics and Chemistry of Solids* **1**, 249 (1957).
 - [65] J. M. Ziman, *Principles of the Theory of Solids*, 2nd ed. (Cambridge University Press, 1972).
 - [66] T. Maeda, H. Hattori, W. H. Chang, Y. Arai, and K. Kinoshita, Hole Hall mobility of SiGe alloys grown by the traveling liquidus-zone method, *Applied Physics Letters* **107**, 152104 (2015).
 - [67] J. Cha, C. Zhou, S.-P. Cho, S. H. Park, and I. Chung, Ultrahigh Power Factor and Electron Mobility in n-Type Bi₂ Te₃ - x %Cu Stabilized under Excess Te Condition, *ACS Applied Materials & Interfaces* **11**, 30999 (2019).
 - [68] Z. Dughaish, Lead telluride as a thermoelectric material for thermoelectric power generation, *Physica B: Condensed Matter* **322**, 205 (2002).
 - [69] H.-S. Kim, Z. M. Gibbs, Y. Tang, H. Wang, and G. J. Snyder, Characterization of Lorenz number with Seebeck coefficient measurement, *APL Materials* **3**, 041506 (2015).
 - [70] E. Flage-Larsen and Ø. Prytz, The Lorenz function: Its properties at optimum thermoelectric figure-of-merit, *Applied Physics Letters* **99**, 202108 (2011).
 - [71] D. M. Zayachuk, The dominant mechanisms of charge-carrier scattering in lead telluride, *Semiconductors* **31**, 173 (1997).
 - [72] J. Cao, J. D. Querales-Flores, A. R. Murphy, S. Fahy, and I. Savić, Dominant electron-phonon scattering mechanisms in n -type PbTe from first principles, *Physical Review B* **98**, 205202 (2018).
 - [73] A. K. Hauble, M. Y. Toriyama, S. Bartling, A. M. Abdel-Mageed, G. J. Snyder, and S. M. Kauzlarich, Experiment and Theory in Concert To Unravel the Remarkable Electronic Properties of Na-Doped Eu₁₁ Zn₄ Sn₂ As₁₂ : A Layered Zintl Phase, *Chemistry of Materials* **35**, 7719 (2023).
 - [74] J. M. Ziman, *Electrons and Phonons: The Theory of Transport Phenomena in Solids* (Clarendon Press, Oxford, 1960).
 - [75] B. Xu and M. J. Verstraete, First Principles Explanation of the Positive Seebeck Coefficient of Lithium, *Physical Review Letters* **112**, 196603 (2014).
 - [76] Y. Xia, J. Park, F. Zhou, and V. Ozoliņš, High Thermoelectric Power Factor in Intermetallic Co Si Arising from Energy Filtering of Electrons by Phonon Scattering, *Physical Review Applied* **11**, 024017 (2019).
 - [77] For technical reasons, the cumulative κ_ℓ was taken from the calculation using $25 \times 25 \times 25$ q -points and hence does not add up exactly to the extrapolated values at 300 K in Fig. 9(b).
 - [78] A. M. Hofmeister, Pressure dependence of thermal transport properties, *Proceedings of the National Academy of Sciences* **104**, 9192 (2007).
 - [79] N. K. Ravichandran and D. Broido, Non-monotonic pressure dependence of the thermal conductivity of boron arsenide, *Nature Communications* **10**, 827 (2019).
 - [80] S. Li, Z. Qin, H. Wu, M. Li, M. Kunz, A. Alatas, A. Kavner, and Y. Hu, Anomalous thermal transport under high pressure in boron arsenide, *Nature* **612**, 459 (2022).
 - [81] O. Cherniushok, T. Parashchuk, R. Cardoso-Gil, Y. Grin, and K. T. Wojciechowski, Controlled Phonon Transport via Chemical Bond Stretching and Defect Engineering: The Case Study of Filled β -Mn-Type Phases, *Inorganic Chemistry* **63**, 18030 (2024).
 - [82] L. Lindsay, D. A. Broido, J. Carrete, N. Mingo, and T. L. Reinecke, Anomalous pressure dependence of thermal conductivities of large mass ratio compounds, *Physical Review B* **91**, 121202 (2015).
 - [83] Q. Lou, Z. Gao, S. Han, F. Liu, C. Fu, and T. Zhu, High Defect Tolerance in Heavy-Band Thermoelectrics, *Advanced Energy Materials* , 2402399 (2024).
 - [84] A. Zevalkink, G. S. Pomrehn, S. Johnson, J. Swallow,

- Z. M. Gibbs, and G. J. Snyder, Influence of the Trier Elements ($M = \text{Al, Ga, In}$) on the Transport Properties of $\text{Ca}_5 M_2 \text{Sb}_6$ Zintl Compounds, *Chemistry of Materials* **24**, 2091 (2012).
- [85] J. Shuai, Y. Wang, Z. Liu, H. S. Kim, J. Mao, J. Sui, and Z. Ren, Enhancement of thermoelectric performance of phase pure Zintl compounds Ca1-Yb Zn2Sb2 , Ca1-Eu Zn2Sb2 , and Eu1-Yb Zn2Sb2 by mechanical alloying and hot pressing, *Nano Energy* **25**, 136 (2016).
- [86] A. She, Y. Sun, Y. Zhao, J. Ni, S. Meng, and Z. Dai, Transport and thermoelectric properties of strongly anharmonic Full-Heusler compounds CsK2M ($M=\text{As, Bi}$), *Materials Today Communications* **34**, 105134 (2023).

Appendix S1: Running average

The running average electron velocity as a function of velocity is calculated as

$$\langle |\mathbf{v}_{n\mathbf{k}}| \rangle(\varepsilon) = \frac{\sum_{n\mathbf{k}} |\mathbf{v}_{n\mathbf{k}}| e^{-\frac{(\varepsilon - \varepsilon_{n\mathbf{k}})^2}{2\sigma^2}}}{\sum_{n\mathbf{k}} e^{-\frac{(\varepsilon - \varepsilon_{n\mathbf{k}})^2}{2\sigma^2}}}, \quad (\text{S1})$$

where $\mathbf{v}_{n\mathbf{k}}$ is the velocity and $\varepsilon_{n\mathbf{k}}$ is the energy at a given k-point \mathbf{k} and band n . The standard deviation σ was chosen to 0.01 eV.

Appendix S2: Deformation potential

TABLE S2. Unique elements of deformation potential for valence band and conduction bands at the Γ and X points at various strain. The superscripts v and c indicate valence and conduction band at Γ or X. The subscript indicates the tensor element of the deformation potential.

Strain	0%	1%	2%	3%	4%	5%
$D_{11}^{\text{v}\Gamma}$ [eV]	1.69	1.68	1.68	1.67	1.67	1.67
$D_{12}^{\text{v}\Gamma}$ [eV]	1.10	1.14	1.18	1.24	1.29	1.34
$D_{11}^{\text{c}\Gamma}$ [eV]	2.42	2.66	2.91	3.18	3.44	3.62
$D_{12}^{\text{c}\Gamma}$ [eV]	0.06	0.06	0.07	0.06	0.03	0.06
$D_{11}^{\text{v}X}$ [eV]	0.59	0.54	0.50	0.44	0.39	0.34
$D_{12}^{\text{v}X}$ [eV]	0.06	0.06	0.06	0.06	0.09	0.08
$D_{13}^{\text{v}X}$ [eV]	0.04	0.04	0.05	0.04	0.01	0.02
$D_{33}^{\text{v}X}$ [eV]	2.67	2.68	2.70	2.71	2.73	2.75
$D_{11}^{\text{c}X}$ [eV]	1.19	1.25	1.33	1.42	1.51	1.60
$D_{12}^{\text{c}X}$ [eV]	0.10	0.08	0.09	0.08	0.05	0.06
$D_{13}^{\text{c}X}$ [eV]	0.02	0.02	0.03	0.02	0.01	0.02
$D_{33}^{\text{c}X}$ [eV]	2.43	2.38	2.34	2.28	2.21	2.14

Appendix S3: Band structure aligned at lowest energy

Appendix S4: HSE06 band structure

**Appendix S5: Transport properties at 300 K and
500 K**

**Appendix S6: k-point and interpolation factor
convergence**

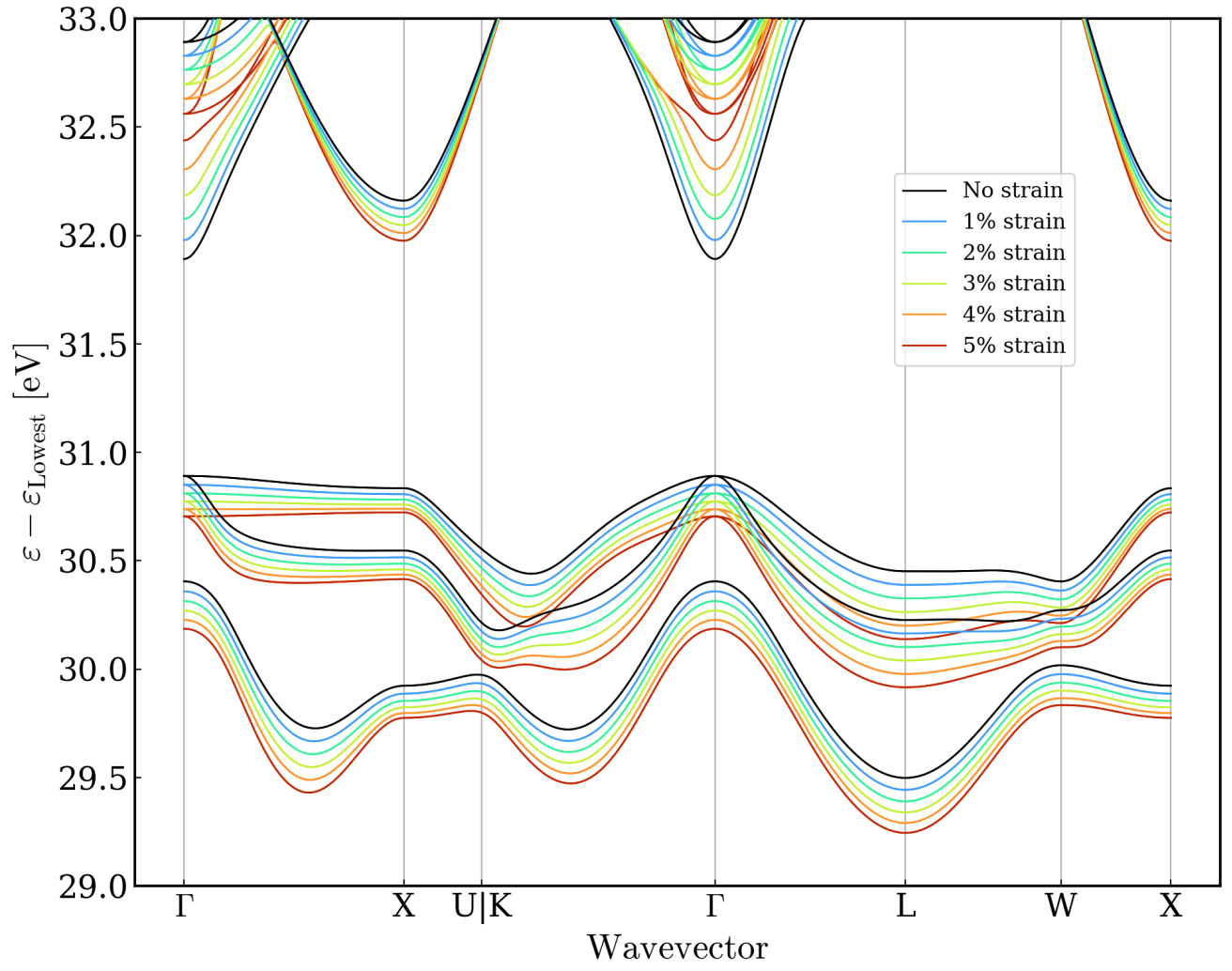


FIG. S11. Band structures of CsK₂Sb at different strains. The lowest energy level of each band structure have been aligned.

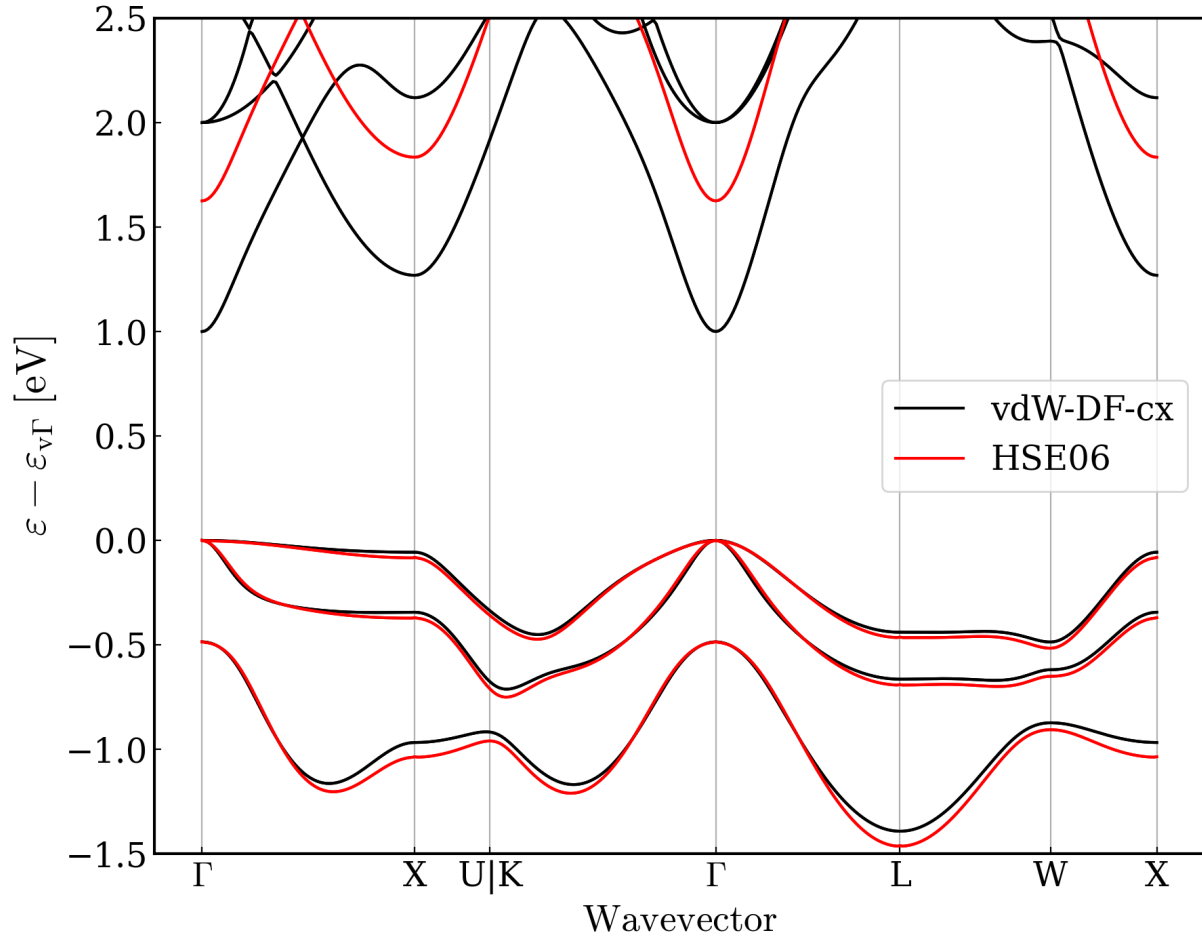


FIG. S12. Band structure of CsK₂Sb plotted with hybrid functional HSE06 in red and vdW-DF-cx black.

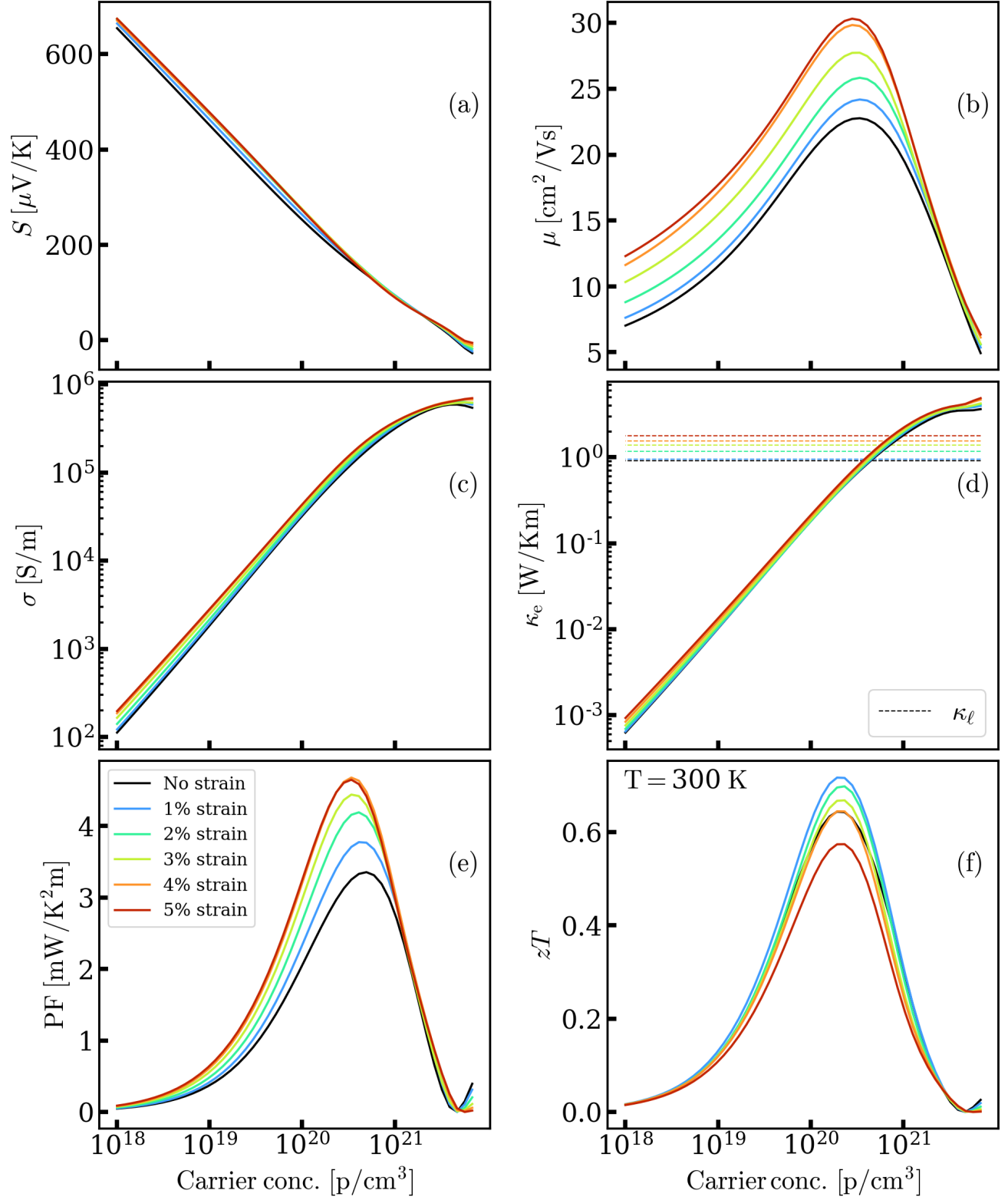
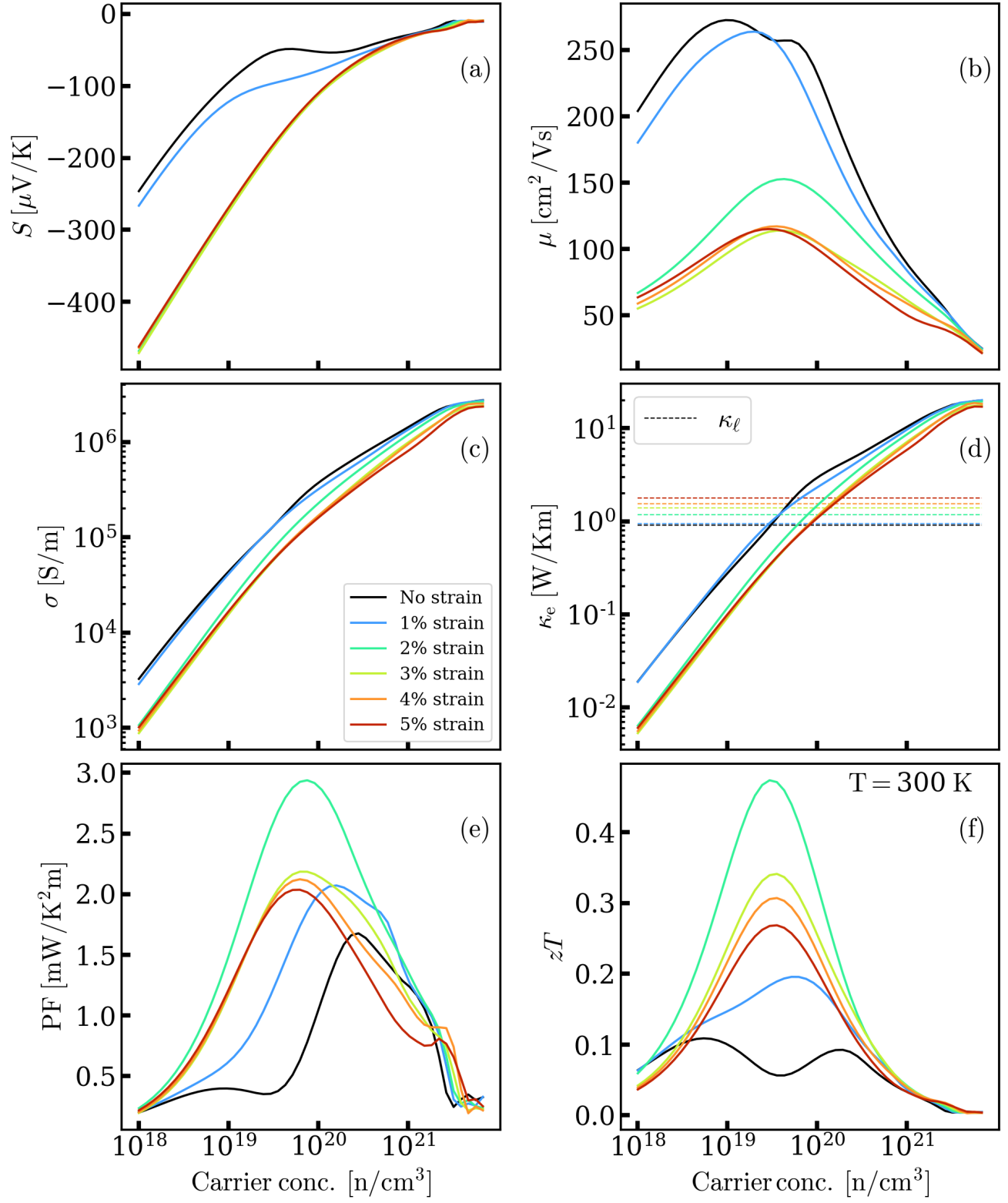
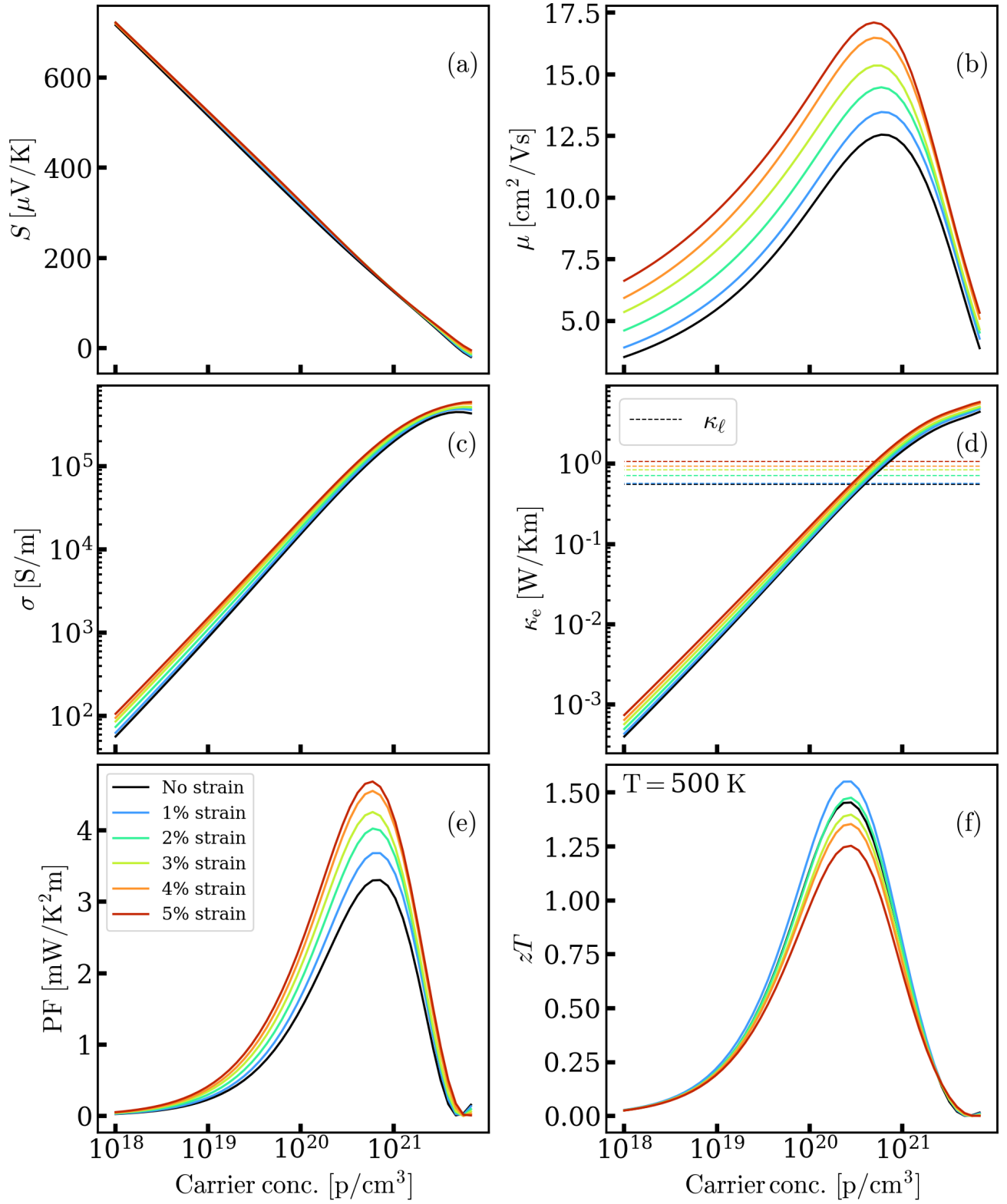
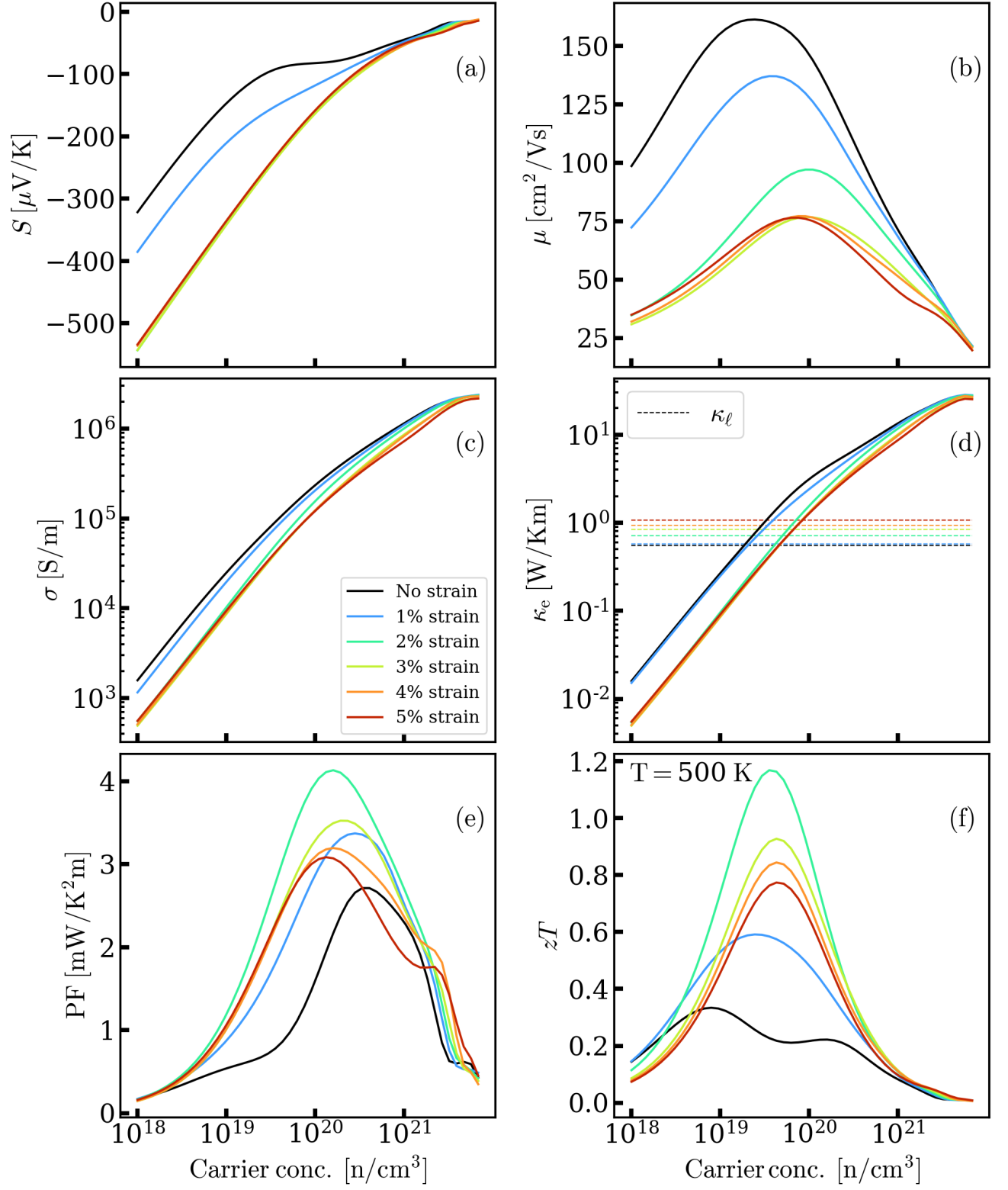


FIG. S13. Seebeck coefficient (S), mobility (μ), conductivity (σ), electron thermal conductivity (κ_e), power factor (PF), and figure of merit (zT) of p-type CsK₂Sb at 300 K.

FIG. S14. Thermoelectric properties of n-type CsK_2Sb at 300 K.

FIG. S15. Thermoelectric properties of p-type CsK_2Sb at 500 K.

FIG. S16. Thermoelectric properties of n-type CsK₂Sb at 500 K.

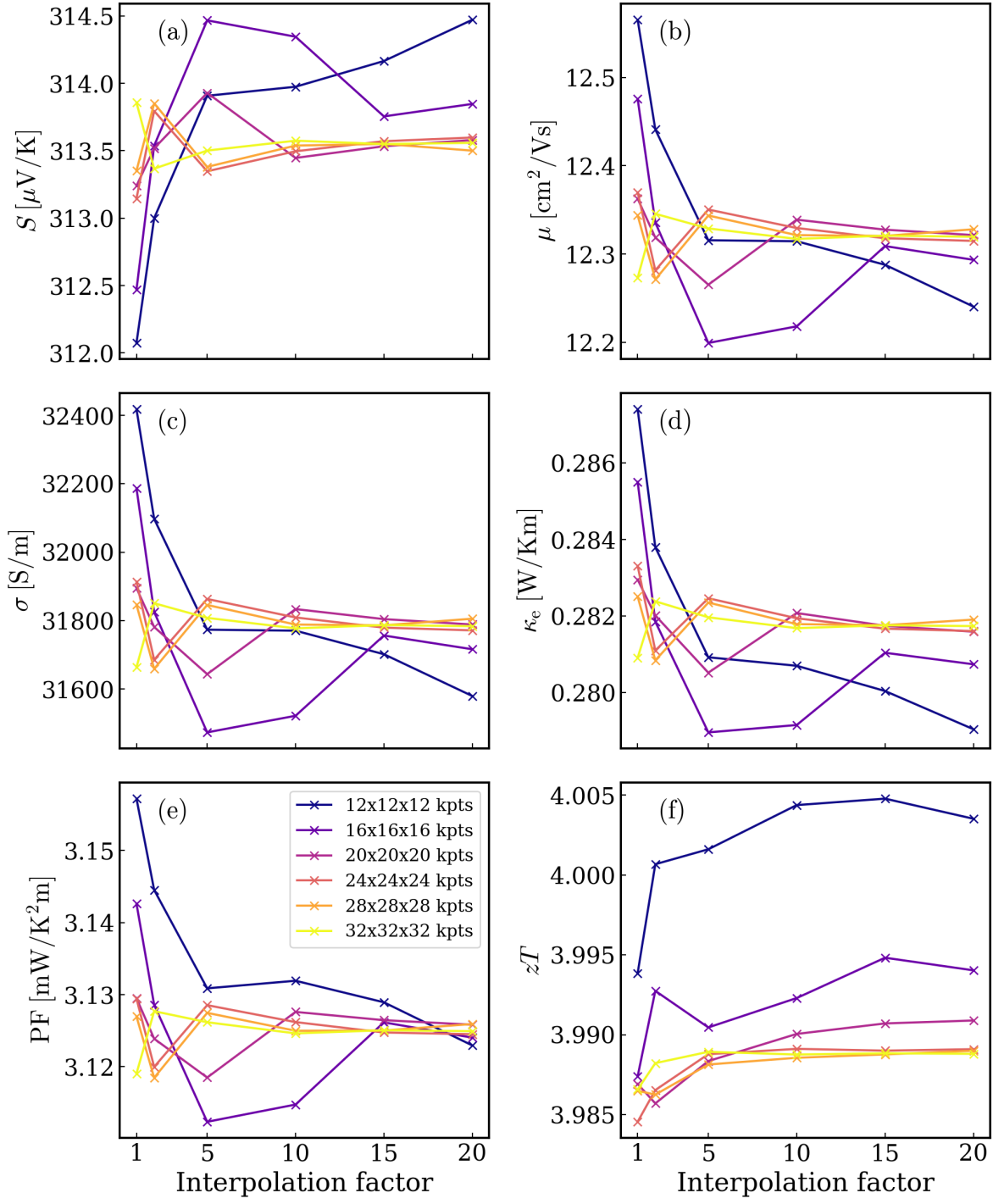


FIG. S17. Constant relaxation time electronic transport properties of p-type CsK₂Sb with interpolation factor 1, 2, 5, 10, 15, and 20. Each line represents a density functional theory calculation with different k-point grid. The properties are at the carrier concentration resulting in maximum zT , $N = 1.61 \times 10^{20}$ p/cm³. A constant relaxation time of 10 fs was used.

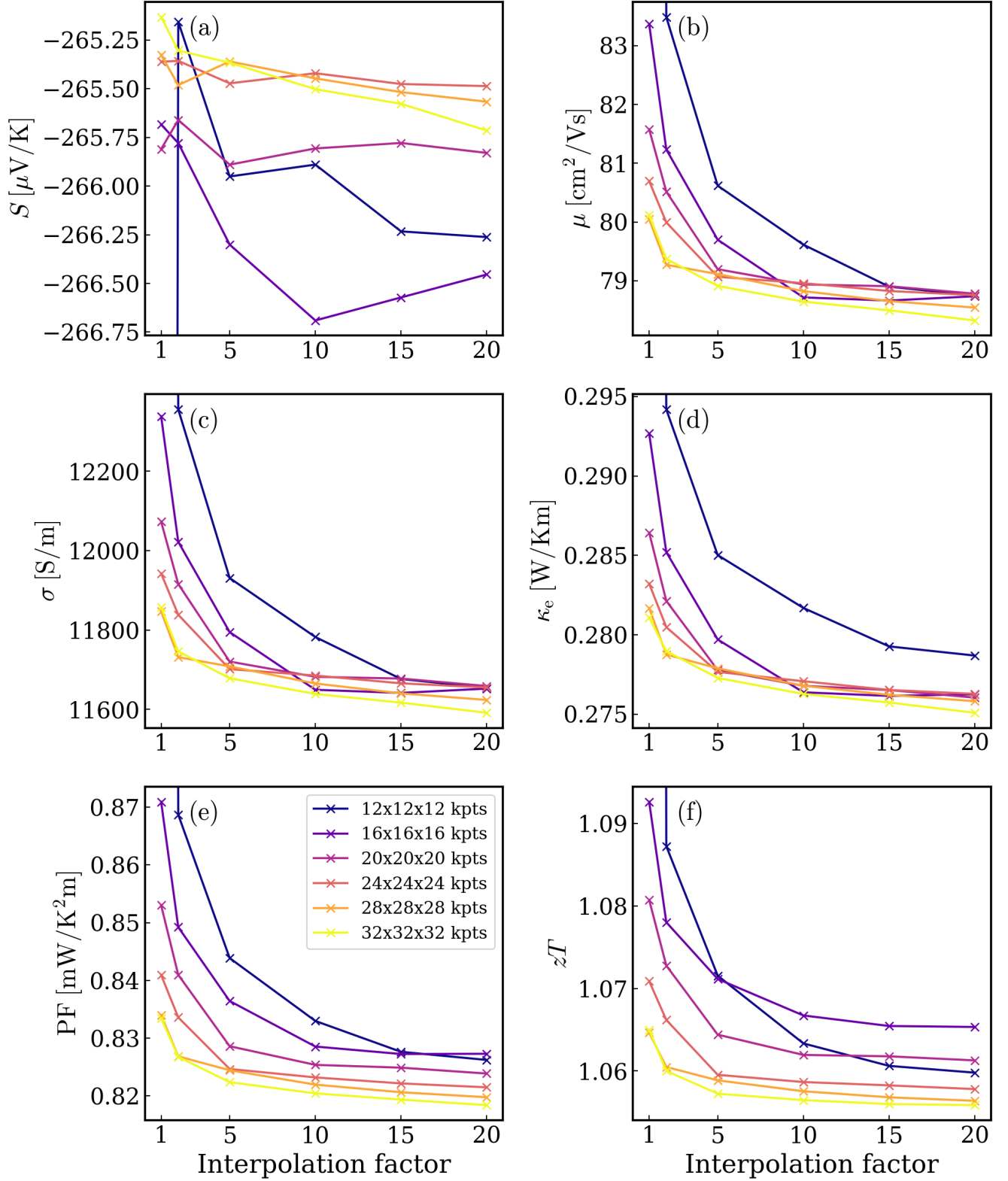


FIG. S18. Constant relaxation time electronic transport properties of n-type CsK₂Sb with interpolation factor 1, 2, 5, 10, 15, and 20. Each line represents DFT calculations with different k-point grid. The properties are at the carrier concentration resulting in maximum zT , $N = 9.24 \times 10^{18}$ n/cm³. A constant relaxation time of 10 fs was used.

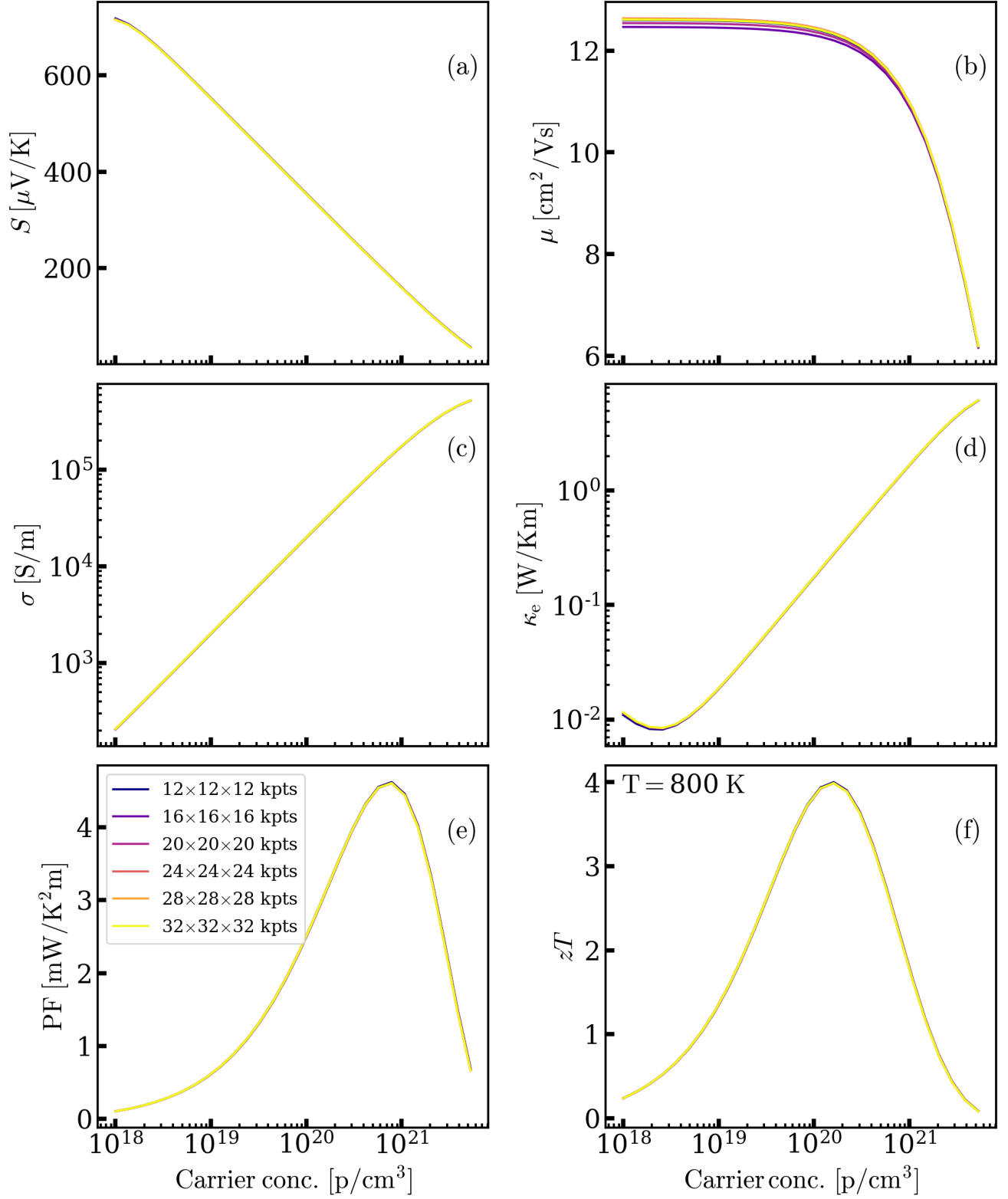
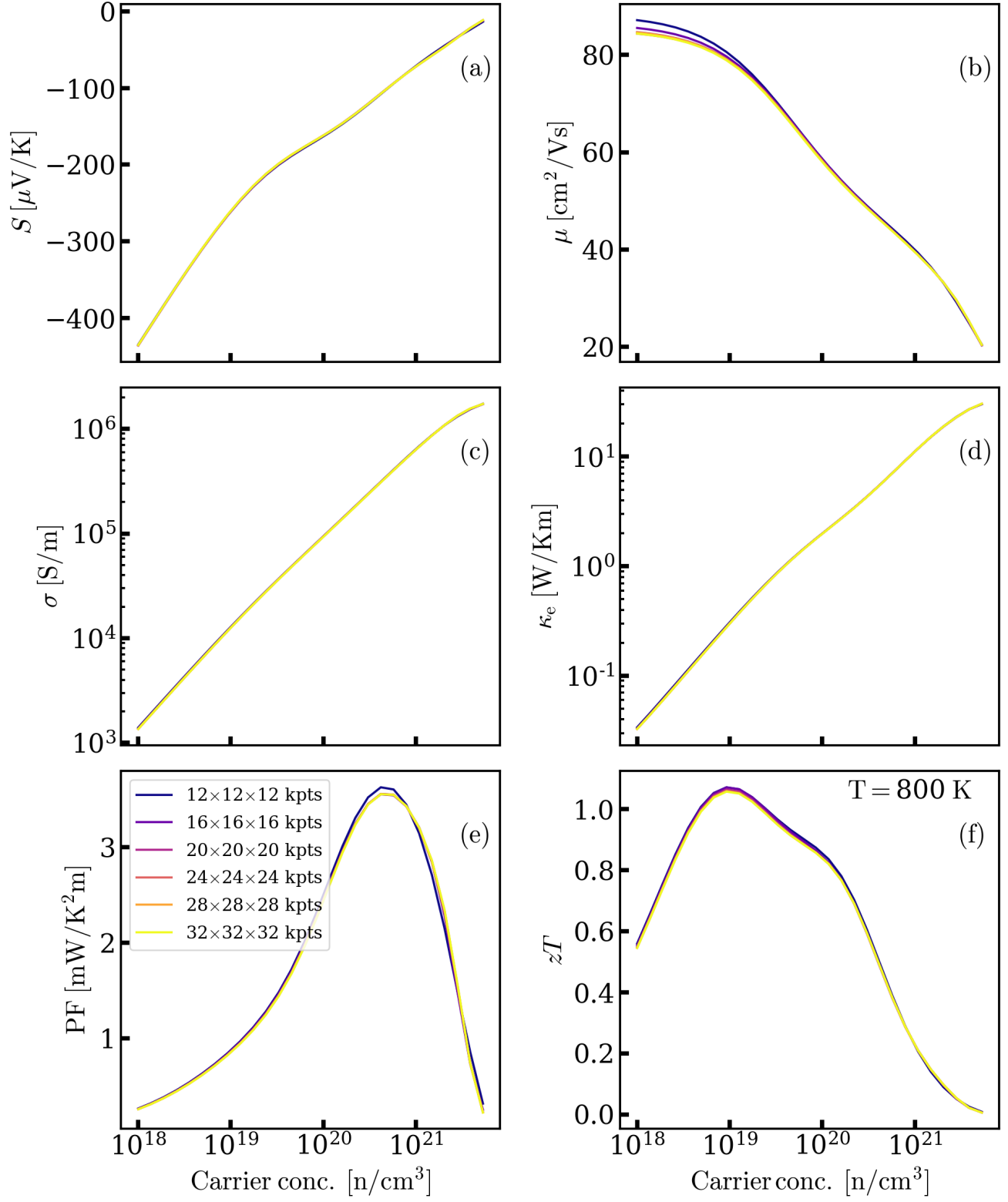


FIG. S19. Constant relaxation time electronic transport properties of p-type CsK₂Sb with different k-points grid and an interpolation factor of 5. A relaxation time of 10 fs was used.

FIG. S20. Constant relaxation time electronic transport properties of p-type CsK_2Sb .